Superradiance Enhanced Magnetic field Detection with NV Centers in Diamond

Shashwat Kumar

A dissertation submitted for the partial fulfilment of BS-MS dual degree in Science

Indian Institute of Science Education and Research Mohali
May 2021

Certificate of Examination

This is to certify that the dissertation titled "Superradiance Enhanced Magnetic field Detection with NV Centers in Diamond" submitted by Shashwat Kumar (Reg. No. MS16064) for the partial fulfilment of BS-MS dual degree programme of the Institute, has been examined by the thesis committee duly appointed by the Institute. The committee finds the work done by the candidate satisfactory and recommends that the report be accepted.
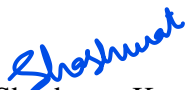

Dr. Kinjalk Lochan   Dr. Manabendra Nath Bera   Dr. Sandeep Goyal
                                                     (Internal Supervisor)

Dated: May 28, 2021

Declaration

The work presented in this dissertation has been carried out by me under the guidance of Dr. Sandeep Goyal (Internal Supervisor) at the Indian Institute of Science Education and Research Mohali, and Dr. Mayeul Chipaux and Prof. Christophe Galland (External Supervisors) at École polytechnique fédérale de Lausanne.

This work has not been submitted in part or in full for a degree, a diploma, or a fellowship to any other university or institute. Whenever contributions of others are involved, every effort is made to indicate this clearly, with due acknowledgement of collaborative research and discussions. This thesis is a bonafide record of original work done by me and all sources listed within have been detailed in the bibliography.

Shashwat Kumar
(Candidate)

Dated: May 28, 2021

In my capacity as the supervisor of the candidate's project work, I certify that the above statements by the candidate are true to the best of my knowledge.

Dr. Mayeul Chipaux   Prof. Christophe Galland   Dr. Sandeep Goyal
(External Supervisor)   (External Supervisor)   (Internal Supervisor)

On May 27th 2021
In Lausanne, Switzerland

Acknowledgements

List of Figures

Notations

NV	Nitrogen Vacancy
ODMR	Optically Detected Magnetic Resonance
VNA	Vector Network Analyzer
ISC	Inter State Crossing
m_s	Spin Quantum Number
PL	Photo-luminescence
ZFS	Zero-field-splitting
ZPL	Zero-phonon-line
PSB	Phonon-side-band
^{14}N	Nitrogen-14
N	Number of Spins
T_1	Spin-lattice relaxation time
T_2	Spin-spin relaxation time
T_2^*	Dephasing time
T	Tesla
σ	Standard Deviation
MW	Microwave
$\vec{B}$	Magnetic Field
SQL	Standard Quantum Limit

Table of Contents

Abstract

We propose the use of entangled Dicke states in a system of large number of spins for enhanced magnetic field sensing. The current magnetic field sensors make use of the non-entangled spins of the diamond NV centers. Which, in principle, keeps the sensing efficiency to be limited by the standard quantum limit (SQL). We harness superradiance from an ensemble of diamond NV centers for generating highly entangled symmetric Dicke states. The use of the symmetric Dicke states for sensing applications could help us get closer to the Heisenberg limit for sensing. Since recently observed superradiance uses a cavity to couple the emission of NV mode to the cavity mode, we open the cavity to detune it from the current emission mode. We give a method to freeze the entangled Dicke states during the superradiant emission from diamond NV centers by detuning the cavity from the emission mode of the Diamond NV centers. Once we have prepared the Dicke states, we can use these states for sensing purpose bounded by Heisenberg limit.

Chapter 1

Introduction

Quantum sensors exploit quantum coherence to detect weak signals with high accuracy and repeat-ability approaching fundamental limits. Among different quantum sensors, nitrogen-vacancy color centers (NV centers) in diamonds have raised a rapid interest due to their capability of optical readout and manipulation of the spins. The use of NV centers as a magnetic field sensor has been demonstrated with both single NVs and NV ensembles [Doherty 13]. This quantum magnetometer has been utilized in many applications such as neuroscience [Hall 12], living system biology [Martínez 20], nuclear magnetic resonance (NMR) vector magnetometry [Maertz 10].

Most of the aforementioned magnetometry applications of the diamond NV centers operate under the standard quantum limit (SQL) of sensing, which originates from the Heisenberg uncertainty principle, giving a fundamental limit to sensing [Barry 20a]. In principle, it is possible to exceed the SQL and to achieve another fundamental limit called Heisenberg limit [Zhou 18], that gives significant edge over sensing with the SQL [Apellaniz 15]. One way to achieve the Heisenberg limit of sensing is to have entanglement among the number of entities in our system [Apellaniz 15], for example, in a spin system as diamond NV centers. Also, the occurrence of superradiance, a phenomenon of collective emission from a system of spins, for example, transits the system through the quantum states that have the entities of the system entangled among each other,

called the Dicke states [Dicke 54]. Diamond NV centers are a perfect system to observe superradiance [Angerer 18] due to their significant coherence times and control by the optical and microwave radiations [Suter 17]. In this thesis, we propose a scheme to get closer to the Heisenberg limit experimentally with diamond NV centers.

Observation of superradiance with diamond NV centers makes use of a resonator to couple the microwave emission mode of the diamond NV centers to the mode of the cavity [Angerer 18]. Superradiance is the phenomenon of collective emission among the spins in the proximity of the emission wavelength. During the superradiant emission, the joint spin system walks down the ladder of entangled states consisting of the collective-spin states called the Dicke states [Dicke 54]. The most symmetric Dicke state occurs for zero eigenvalues of the Z component of the spin angular momentum operator. Among all the Dicke states, this state is the most susceptible to an external perturbation, like a magnetic field in our case. We make use of this state for improving the sensitivity of the NV center based magnetometer. For preparing the Dicke states, we propose to detune the cavity from the emission frequency of diamond NV centers during the middle of the superradiant emission with the help of a switch. With symmetric Dicke state for sensing purpose, we aim to improve the magnetic field sensitivity by using entanglement among the spin.

In chapter 2, we give an introduction to NV defect centers in diamond. We discuss the electronic, optical and magnetic properties of the NV centers. We also review the already observed superradiance in the chapter. Chapter 3 is about the NV sample characterization and magnetic field detection techniques like ODMR, Rabi, Ramsey, and Hahn Echo experiments. We also discuss the standard quantum limit (SQL) of sensing. In chapter 4, we propose our scheme of magnetic field sensing with Dicke states. Our proposal promises sensing close to the Heisenberg limit with diamond NV centers. We present the ongoing experiments, cavity fabrication, and conclusion to the thesis in chapter 5.

As magnetometry with entangled states would give better sensing than the existing magnetometers [Apellaniz 15], it would have direct applications in better sensing and detecting the sub cellular magnetic particles inside a cell as already demonstrated with the typical magnetometers [Kuwahata 20], consequently having biomedical applications. The other advantages of the advanced sensing would include metrology applications and imaging of neural activities in brain, as demonstrated with typical diamond NV magnetometers [Doherty 14, Karadas 18].

Chapter 2

The NV Defect Centers in Diamond

The NV color centers in diamond are an excellent system to observe the quantum phenomenon like Spin-orbit coupling and Zeeman splitting, that are used in quantum sensing and information processing [Suter 17, Doherty 13]. Recently, the phenomenon of collective emission, superradiance, has been observed in the NV centers [Angerer 18], that we propose to use for the sensing purpose by "freezing" the Dicke states that the system go through during the superradiant emission [Dicke 54]. In this chapter, we will give an introduction to diamond NV centers and their optical and electronic properties, and manifestation of physical phenomenon like Zeeman Splitting and use of the same for spin manipulation [Suter 17, Doherty 13]. Further, we also explain the phenomena of superradiance and its manifestation with diamond NV centers [Angerer 18, Dicke 54].

The NV centers are one of the many point defects present in diamond [Zaitsev 00]. At a carbon site in the diamond lattice, the two neighbouring carbon atoms are replaced by a Nitrogen atom and an absence of any atom, also called a vacancy as shown in figure 2.1 (a). This arrangement leaves the one electron of the Nitrogen atom unpaired, and the system is called NV^0. This configuration alters the energy structure within the crystal such that NV^0 could capture a free electron from the conduction band, forming the negatively charged NV^- [Doherty 13]. Another charged state of NV center is NV^+, which corre-

spond to the positive charged states of the vacancy center, and the modification from one type of charged state of the NV center to another can be done with the help of a tunable laser [Aslam 13]. Out of these, NV^- is the most suitable for magnetometry and information processing [Doherty 13]. For making the rest of the text simple, we will call the negatively charged NV^- as the 'NV center'.The symmetry axis of the NV center is always in the one of the four [111] crystallographic orientations.

2.1   Electronic Structure of Diamond NV Centers

NV center has a spin-1 triplet ground state, the most useful state of magnetometry purposes, $^3A_2$, with significantly long spin lifetimes at room temperatures [Jarmola 12]. The energy levels of the NV center are named according to the irreducible representation of the C_{3V} symmetry group of the NV defect center, A_1, A_2, and E, and the superscript represents the number of allowed m_s spin states [Chu 15]. As shown in figure 2.1b, the $^3A_2$ ground state connects to the triplet excited state ^3E by an energy of 1.945 eV (637 nm) as shown in figure 2.1. The system is driven with a green laser of 532 nm or 2.33 eV that would drive the system above the ^3E state keeping the spin state intact [Suter 17]. When there is no external magnetic field, the ground state $^3A_2$ splits into two magnetic spin states, $m_s = 0$ and degenerate $m_s = +1$ and $m_s = -1$ ($m_s = \pm 1$) states.

The two spin ground states $^3A_2$ $m_s = 0$ and $m_s = \pm 1$ have a Zero field splitting (ZFS) due to the spin-spin interaction among the electrons of the NV center because of a tight confinement in the non cubic diamond lattice. The excited state ^3E of the NV center possesses a similar electronic structure that also has a smaller ZFS arising due to the spin orbit coupling in the excited state [Doherty 13, Suter 17]. The other singlet states $^1A_1$ and ^1E, also called shelving

states, stem from the intrinsic configuration of the NV center and corresponds to the non radiative inter system crossing (ISC), that involves the transition between the two states with different spin multiplicity (in case of NV centers, the transition from a triplet state to a singlet state) [Suter 17].
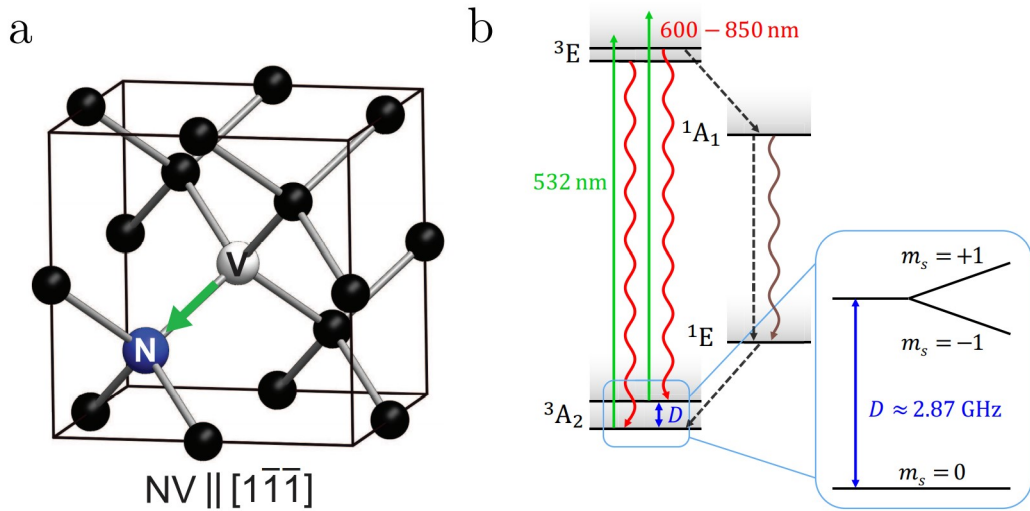
Figure 2.1: The figure is adapted from [Barry 20a], demonstrating the NV center quantum system. a) NV center in the diamond lattice, showing the vacancy and the presence of the Nitrogen atom. The NV symmetric axis is shown by the green arrow along the particular axis. b) It shows the energy level diagram for the NV$^-$ color center in diamond. The state of interest is the ground state ^{3}A$_2$

2.2   Optical properties of the NV center

The NV center is excited with a green laser of 532 nm to transfer the electrons from the ground to the excited state. The ^{3}A$_2$ ground state connects to the triplet excited state ^{3}E by an energy of 1.945 eV (637 nm) as shown in figure 2.1. The system is driven with a green laser of 532 nm or 2.33 eV that would drive the system well above the ^{3}E state from where it nonradiatively relaxes to ^{3}E state quickly, keeping the spin state intact [Suter 17]. This tran-

sition conserves the spin, that is, the ground $m_s = 0$ and $m_s = \pm 1$ states go to excited $m_s = 0$ and $m_s = \pm 1$ states respectively [Doherty 13]. In both the cases, the electron is allowed to decay back by emitting a red photon corresponding to the energy gap of 1.945 eV or 637nm as shown in figure 2.1b.
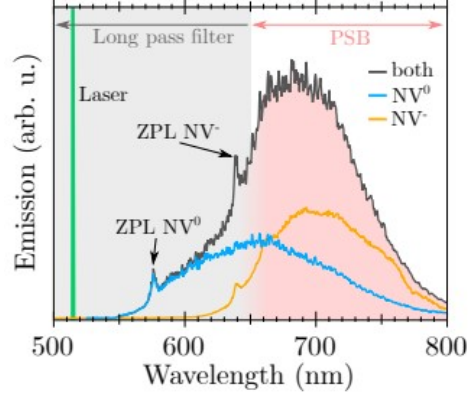
Figure 2.2: Fluorescence spectra (in arbitrary units) of NV^0, NV^-, and total at excitation with a green laser. Both the charged states have unique contribution to the total fluorescence signal corresponding to their respective zero phonon lines and phonon sidebands. The proper choice of filters concentrates the spectroscopy on the signal corresponding to NV^- (adaptation from [Qnami 20]).

The direct optical transition comes with the phonon assisted spectrum known as the phonon sideband producing fluorescence between 600 nm and 850 nm [Barry 20a] as shown in figure 2.2. The spectrum consists of the zero phonon lines (ZPL) and the phonon side bands (PSB) of the two charged states. A long pass filter that selects the emission beyond 650 nm would allow us to target the signal corresponding to NV^- only. The photostability of the defect over time also make it an excellent single photon source [Rondin 14].

There are two ways to go from the excited state ^3E to $^3A_2$ ground state: the excited $m_s = 0$ state mostly relaxes to the ground state $m_s = 0$, while the excited $m_s = \pm 1$ state, along with direct transition to the $m_s = \pm 1$ ground state, would cross over through the singlet states $^1A_1$ and ^1E. This intersystem crossing (ISC) is non radiative and would often lead the system in the $m_s = 0$ ground state(30% branching ratio) [Suter 17]. Which has two important ap-

plications, 1) the initialisation of the NV center in a known spin state (ground $m_s = 0$), 2) reading out the spin state optically during experiments [Barry 20a].

2.3 The spin-state initialization

As the excitation process of the NV center is with a green laser, the continuous laser application would make many excitation and emission cycles. As we saw in last section, the emission from the ^{3}E $m_s = \pm 1$ excited state goes through the singlet states via nonradiative intersystem crossing and affects the population of the ground state ^{3}A$_2$. In the radiative process of decay, the electrons from the ground states ^{3}A$_2$ $m_s = 0$ and $m_s = \pm 1$ would return to their initial states after the radiative cycle. However, due to the extra decay mechanism (ISC) passing through the singlet states ^{1}A$_1$ and ^{1}E would eventually transfer the population from ground ^{3}A$_2$ $m_s = \pm 1$ to $m_s = 0$ state. This is because the ISC originating from excited ^{3}E $m_s = \pm 1$ almost decays exclusively to ground $m_s = 0$ state. Hence, normally shining green light on the NV system that cycles through many of these transitions would progressively prepare the spin population in to the ground ^{3}A$_2$ $m_s = 0$ state. After a few microseconds, the NV system is initialized in a known ground $m_s = 0$ state with a fidelity near 90% [Suter 17].

2.4 Spin state readout

Since there is a competing non radiative decay path corresponding to excited ^{3}E $m_s = \pm 1$ state, there is a difference in the photoluminescence (PL) of the ground $m_s = 0$ (bright) and $m_s = \pm 1$ (reduced intensity or dark) ground states. Hence, by simply checking the PL of the NV system [Suter 17]. As we are

interested in the ground state $^3A_2$ of the NV center, we call $m_s = 0$ as the bright state, and $m_s = \pm 1$ as the dark state, and polarization means bringing spins to the $m_s = 0$ state.

2.5   Spin-state manipulation

As discussed in the last section, the NV's $^3A_2$ ground state's spin triplets $m_s = 0$ and $m_s = \pm 1$ are useful for the magnetometry purposes [Suter 17]. As seen in section 2.1, there is a zero field splitting (ZFS) of 2.87 GHz between $m_s = 0$ and $m_s = \pm 1$ states in the absence of an external magnetic field, which falls in the microwave regime of the electromagnetic radiation. Hence, after polarization, by applying a microwave pulse at 2.87 GHz would send the spins from $m_s = 0$ to $m_s = \pm 1$ state [Suter 17, Barry 20a, Rondin 14]. One example demonstrating this effect is Optically Detected Magnetic Resonance (ODMR) where the NV fluorescence with continuous laser excitation is observed as a function of the applied microwave frequency [Suter 17], an example of continuous wave (CW) experiment. When the applied microwave frequency is equal to the resonance frequency, in absence of an external magnetic field with ZFS = 2.87 GHz, there is a dip in the NV fluorescence, that is the population transfers from $m_s = 0$ (bright) to $m_s = \pm 1$ (dark) state. In case of the continuous wave (CW) experiment we discussed, the amount of transfer to $m_s = \pm 1$ state depends on the laser power of the applied laser and the microwave power of the microwave radiation during ODMR [Qnami 20]. For a single NV, the maximum possible contrast of the fluorescence dip is close to 30% [Suter 17] which is a consequence of the overall decay rates as shown in figure 2.3. The width of the resonance dip is limited by the coherence time T_2^* of the NV system, which is the time constant inherent to the sample determining the rate at which the in-phase spins would go out of phase among each other [Suter 17].
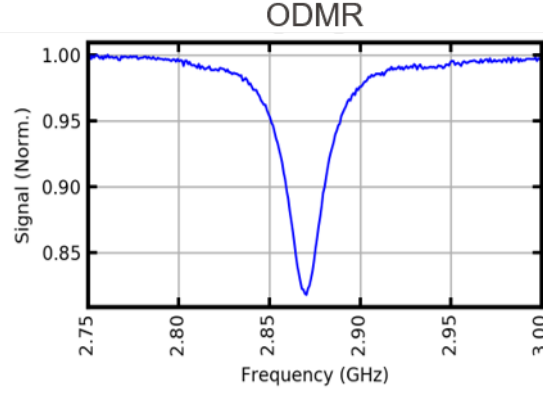
Figure 2.3: ODMR: NV fluorescence as a function of applied microwave frequency. There is a dip at 2.87 GHz corresponding to the Zero field splitting. The X-axis represents the applied frequency and the Y-axis is the normalized signal. The contrast is close to 20%.

Moreover, when we have the need of the pulsed excitation, we have the freedom of choosing the population transfer precisely. And, an arbitrary superposition of the system's states can be created by managing the pulse length of the microwave signal [Suter 17]. This property of NV centers can be used to estimate the quantum character of the color center by performing advanced experiments like Rabi, Ramsey, and Hahn Echo sequences [Doherty 13] that we will see in the next chapters.

2.6 Zeeman effect with NV centers

Working with NV centers is possible due to very interesting optical properties of the ground state $^3A_2$ in figure 3.15 [Barry 20a]. The ground state is a triplet with $m_s = \pm 1$ state degenerate at the zero magnetic field. Applying an external magnetic field would lift the degeneracy, and the splitting is proportional to the gyromagnetic ratio and the strength of the magnetic field [Suter 17]. The $m_s = 0$ state is not affected by the magnetic field as it is not degenerate. When

we apply a green laser of 532 nm, the system goes to the excited state ^{3}E. As mentioned above, it has two ways to come back, the first one is to emit a red photon (600-850nm) and directly go to the ground state ^{3}A$_2$. The other way is to relax by an inter-system-crossing (ISC) way via the singlet ^{1}A and ^{1}E states. This way, in the ground state ^{3}A$_2$, we can polarize electrons from the $m_s = \pm 1$ states to the $m_s = 0$ state. Once the electrons are polarized to the ground $m_s = 0$ state, we can drive these spins with the Microwave pulses at 2.87 GHz at zero field. We do measurements like Rabi oscillations to find a π pulse and drive the spins almost completely from $m_s = 0$ state to $m_s = \pm 1$ state [Barry 20a].

If there is an external magnetic field present, the $m_s = \pm 1$ is further split, and it is easily observed in the Optically Detected Magnetic Resonance (ODMR), which makes use of both the optical and the microwave properties of the diamond NV centers to find the splitting in the $m_s = \pm 1$ states.

Let's first concentrate on a single NV center, the Hamiltonian of the ground state in the NV centers with electron spin $\vec{S}$ (S=1), can be written as [Suter 17],

$$H_s = DS_z^2 - \gamma_e j \vec{B}_0 . \vec{S}$$

where, S_z is the Z component of electron spin $\vec{S}$, and the zero field splitting is given by D = 2.870 GHz, and the gyromagnetic ratio $\gamma_e = -28.02 GHz/T$ [Suter 17], and $\vec{B}_0$ is the magnetic field along the symmetric axis of the NV centers.

A single NV center is split into two resonance peaks when an external magnetic field is applied, given by the expression $2\gamma_e B_z$ corresponding to the Zeeman splitting due to an external magnetic field [Suter 17]. It's one of the ways to calculate the external magnetic field.
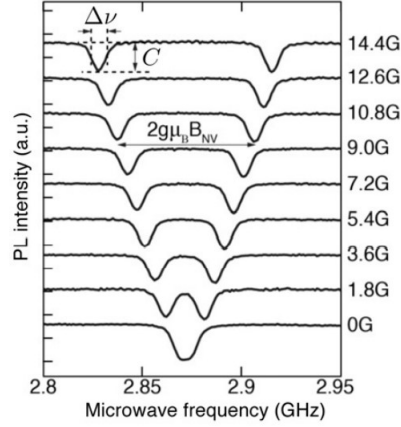
Figure 2.4: Splitting of the ODMR lines with different values of the magnetic fields. The splitting depends on the applied field along the NV axis B_{NV} and the gyromagnetic ratio. The width of the splitting $\Delta\nu$ gives the information about the inhomogenous broadening (T_2) of the system, and C is the contrast. The figure is taken from [Rondin 14]

In figure 2.4 shows the splitting of the ODMR dips with varying values of the magnetic field along the NV axis in a single NV center.

2.6.1 ^{14}N Hyperfine Splitting

In a sample, every center shows a hyperfine splitting [Suter 17] due to the adjacent I =1 ^{14}N nuclear spins, which split each ODMR dip into further three splittings, as shown in figure 2.5. Due to the 3-fold rotational symmetry of the NV centers, the hyperfine interactions with the ^{14}N is axially symmetric, taking the form as [Suter 17],

$$H_{hfN} = A_{||}I_z S_z + A_{\perp}(I_+ S_- + I_- S_+)$$

Where A's are the hyperfine coupling constants, in the respective orientations, and I and S are the nuclear spin and electron's spin operators respectively. The first term in the above Hamiltonian commutes with the Hamiltonian of the zero

field $H_{ZF} = DS_z^2$, due to which, it has a dominant effect in the energy spectrum, with the longitudinal component $A_{||} = -2.15MHz$. While the term containing the transverse component $A_\perp$ doesn't commute with the zero field Hamiltonian and doesn't have an effect in the Hyperfine splitting [Suter 17].
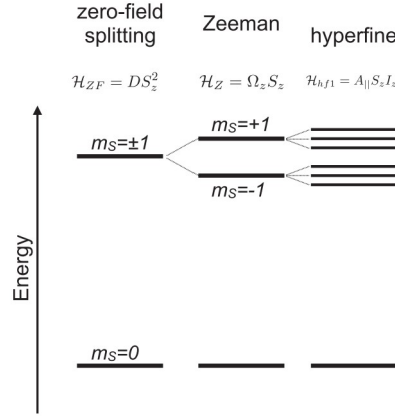
Figure 2.5: Splitting in the electron's energy level due to different terms in the Hamiltonian, giving rise to hyperfine splitting due to ^{14}N. The figure is taken from [Suter 17]

With the discussed physics of spin dynamics of NV center in this chapter, we can understand the advanced pulsed experiments like Rabi oscillations, Ramsey sequence, Hahn Echo, and T_1 experiments [Doherty 13]. We shall see these experiments in the upcoming chapters.

2.7 Superradiance

Superradiance is a phenomena of radiation enhancement among a group of large number of emitters that interact with a common light field [Dicke 54]. It is different than the ordinary fluorescence as in ordinary fluorescence, the emitters can be understood interacting independently with the radiation field, and emission follows the exponential law in the decay process, observed in dilute

emitter systems. When the number of emitters in the sample are very large, the emission is much faster and stronger than the emission of independent emitters, also known as the phenomenon of superradiance [Gross 82]. The comparison between fluorescence and superradiance emission profile is shown in figure 2.6.
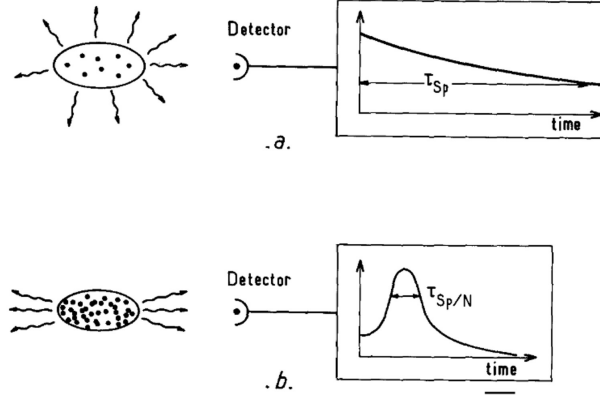
Figure 2.6: Comparision of the emission profile of normal fluorescence (a) and superradiance (b). τ_{sp} is the time constant for the ordinary fluorescence decay. Superradiance decay is faster by a factor of number of emitters N. (Adapted from [Gross 82])

Let's understand this phenomena in optical regime. Consider we have a set of N two-level systems evolving under the effect of different incoherent interactions with their environment. The free Hamiltonian describing N identical and independent two-level systems of energy $\hbar\omega_0$ can then be written in terms of spins as

$$H_0 = \hbar\omega_0 \sum_{n=1}^{N} J_{z,n} = \hbar\omega_0 J_z \tag{2.1}$$

$J_{z,n}$ is the z-spin operator for the nth particle and J_z is the total spin operator.

The interaction Hamiltonian with the electric field **E** in the dipolar approxima-

tion [Shammah 17]

$$H_{int} = \mathbf{d}.\mathbf{E} \sum_{n=1}^{N} (J_{+,n} + J_{-,n}) = \mathbf{d}.\mathbf{E}(J_{+} + J_{-}) \qquad (2.2)$$

here $J_{\pm,n}$ is the ladder operator acting on the nth particle, and $J_{\pm}$ is the total spin operator.

The coupling of the system with the electromagnetic field, and other dephasing factors, can be described by introducing the master equation for the density matrix ρ of the system [Shammah 17],

$$\frac{d\rho}{dt} = i\omega_0[J_z, \rho] + \frac{\gamma_S}{2}\mathscr{L}_{J_-}[\rho] + \frac{\gamma_L}{2}\sum_{n=1}^{N}\mathscr{L}_{J_{-,n}}[\rho] + \frac{\gamma_D}{2}\sum_{n=1}^{N}\mathscr{L}_{J_{z,n}}[\rho] \qquad (2.3)$$

the Lindblad operator $\mathscr{L}_O[\rho] = 2O\rho O^{\dagger} - O^{\dagger}O\rho - \rho O^{\dagger}O$ is describing the different scattering rates quantified by the spontaneous emission rate γ_S, the nonradiative relaxation rate γ_L, and the pure dephasing rate γ_D. We use QuTip [Johansson 12] to solve the master equation [Shammah]. The emission is given by $< J_+ J_- > (t)$ as shown in Fig. 2.7.
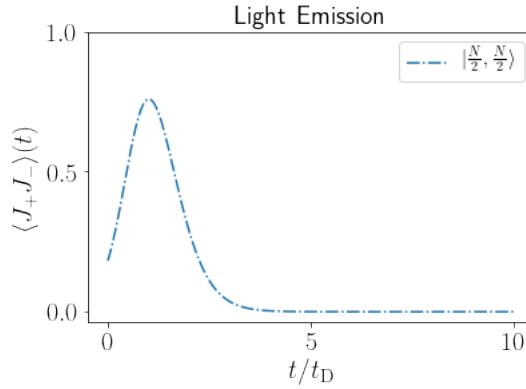
Figure 2.7: **The superradiant emission for 20 spins, initially in the most excited superradiant state.** t_D **is the Collective emission delay time that is used as a reference.**

The superradiant emission profile as shown in figure 2.7 is observed when the number of emitters (spins in the case of NV centers) in the sample are very

large so that the emitters are well within the emission wavelength proximity of each other. In such a case, the collection of emitters start to radiate much stronger and faster than the independent emitters [Gross 82]. Superradiance is due to spontaneous phase-locking of the dipoles throughout the medium, and the radiation intensity is proportional to the square of the number of radiators N and the energy of the system is released within a short radiative burst. During the superradiant emission, the system goes through highly entangled Dicke states [Dicke 54], that we propose to use for magnetic field sensing.

2.8   Superradiance from Diamond NV centers

Superradiance has been observed from the ensembles in diamond NV centers in Microwave regime [Angerer 18]. This observation was possible because of the uniform coupling of the system with the magnetic field mode inside a cavity. The similar cavity is shown in the following figure 2.8,
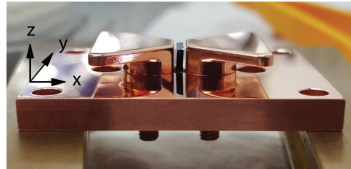
Figure 2.8: Cavity with mounted diamond sample, taken from [Angerer 16]

We need to estimate the cavity parameters in order to proceed in the direction of reproducing the results from this paper. The cavity parameters are estimated as follows.

2.8.1 Cavity Mode Volume

In a microwave cavity, the cavity mode volume corresponds to the spatial confinement of the effective magnetic field inside the cavity [Angerer 16]. The value of mode volume is required for characterizing the cavity and to get the Purcell factor. We analyze the cavity from [Angerer 16] to get the value for cavity mode volume. The expression for single spin coupling strength g_0 to the cavity is [Angerer 16],

$$|g_0| = \sqrt{\frac{2}{3}} \frac{\mu_B g}{2\hbar} \left| \vec{B_{rf}^0} \right| \left| \vec{S} \right|$$
(2.4)

where, μ_B is Bohr magneton, g is Lande's g factor, $\hbar$ is the reduced Planck's constant, $\vec{B_{rf}^0}$ is the quantized magnetic field inside the cavity, and $\vec{S}$ is the spin operator for a single spin. The quantized magnetic field inside the cavity, $\vec{B_{rf}^0}$, is [Putz 17],

$$\vec{B_{rf}^0} = -i \sqrt{\frac{\hbar \omega \mu_0}{2V}} (a - a^\dagger) \cos(kz)$$
(2.5)

here, z is the direction of propagation of the wave, and k is the magnitude of the wave vector, ω is the cavity frequency, μ_0 is the magnetic constant, a is the annihilation operator of the field, and V is cavity mode volume. Hence, for the equation 2.4, we get,

$$\left| \vec{B_{rf}^0} \right| \approx \sqrt{\frac{\hbar \omega \mu_0}{2V}}, \left| \vec{S} \right| \approx 1$$
(2.6)

Therefore, equation 2.4 becomes,

$$|g_0| \approx \sqrt{\frac{2}{3}} \frac{\mu_B g}{2\hbar} \sqrt{\frac{\hbar \omega \mu_0}{2V}} \tag{2.7}$$

which gives,

$$V \approx \frac{\omega \mu_0 g^2 \mu_B^2}{12|g_0|^2 \hbar} \tag{2.8}$$

Taking the value of parameters [Angerer 18] and putting the values of the constants,

$\omega = 3.18 GHz$ (cavity mode frequency)

$\mu_0 = 1.25 \times 10^{-6} mkgs^{-2}A^{-2}$ (the magnetic constant)

$g = 2$ (the Lande's g factor)

$\mu_B = 9.274 \times 10^{-24} J/T$ (Bohr Magneton)

$\hbar = 1.05 \times 10^{-34} m^2 kg/s$ (reduced Planck's constant)

$|g_0| = 50 mHz$ (single-spin coupling)

Putting all these values in equation 2.8,

$$V = 4.34 \times 10^{-7} m^3 \equiv 434(mm)^3 \tag{2.9}$$

The wavelength of electromagnetic mode is $\sim .094m$, and $\frac{\lambda}{2} \sim .047m = 4.7cm$. While, the effective cavity mode length ($V^{\frac{1}{3}} = (434mm)^{\frac{1}{3}}$) is $\sim 7.5mm$. The cavity mode volume is very small as compared to the wavelength of the electromagnetic mode.

The dimensions of the resonator are not given directly [Angerer 16], but the dimensions of the sample are given, which are $4.2mm \times 3.4mm \times 0.92mm$ [Angerer 16]. Which may give an approximation of the mode volume. The dimension of the resonator where the magnetic field is applied looks best to compare

with, Fig 2.9, where we have effective g_0 (coupling).
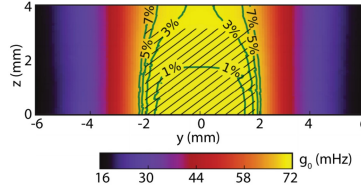
Figure 2.9: Magnetic field distribution. The plot shows a cross section of the mode volume parallel to the direction of the magnetic field mode (y- direction in Fig 2.8), taken from [Angerer 16]

Hence, we find that the cavity mode volume is 434 $(mm)^3$.

2.8.2 Purcell Factor

Purcell factor is the measure of the enhanced spontaneous emission rate of a quantum system (NV centers in our case) by its environment (the cavity). The Purcell factor is given by [wik],

$$F_P = \frac{3}{4\pi^2}(\frac{\lambda_{free}}{n})^3\frac{Q}{V} \qquad (2.10)$$

where, λ_{free} is the wavelength of the cavity mode, n is the refractive index of the material(≈ 1 as it is in air), V and Q are the mode volume and the quality factor respectively.

From [Angerer 18], $Q = 230$, $\lambda = 0.094$m, and $V = 434 \times 10^{-9}m^3$, as calculated in the previous section. Putting these values in equation 2.10, we get,

$$F_P = 33812.9 \qquad (2.11)$$

which is agreeable from reference [Breeze 15]. We shall use the values of these

cavity parameters for the design of our own cavity for the experiment.

2.9   Signature of Superradiance

Experimentally, superradiant emission is observed in the diamond NV centers in Microwave regime. As shown in Fig 2.10, as a π pulse is applied to a number of polarized NV spins, there is a sudden burst of the coherent photon emission near 300 ns [Angerer 18]. As the number of spins is increased and made upto 4 times the initial ones, the intensity of emission changes nonlinearly, as shown in figure 2.11.
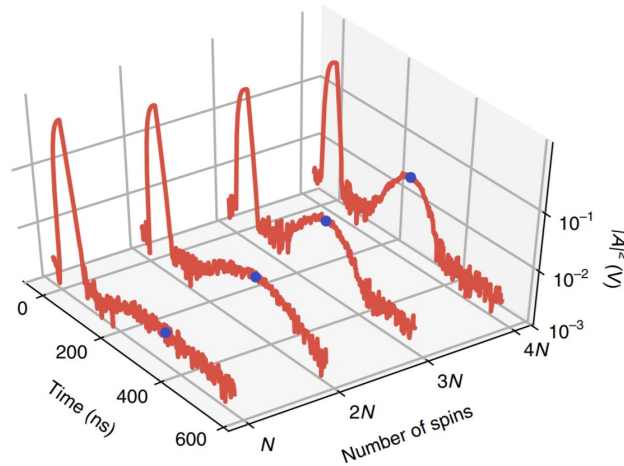
Figure 2.10: By bringing either N, 2N, 3N or 4N spins into resonance with the cavity mode, the dependence of the emitted photon intensity on the number of spins is observed, taken from [Angerer 18]
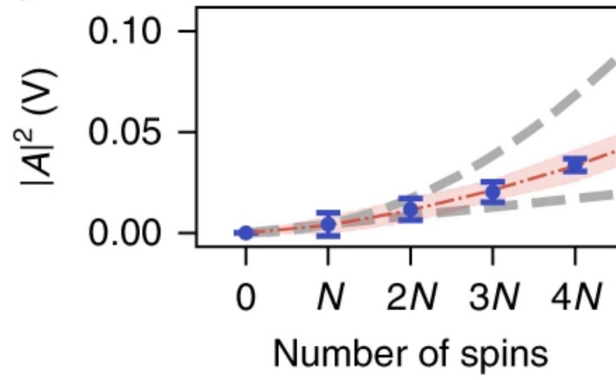
Figure 2.11: Non Linear dependence of emission intensity on the number of spins, taken from [Angerer 18]

As shown in figure 2.11, the observed dependence of the the emission intensity to the number of spins is $N^{1.52}$ while theoretical prediction is N^2. It is due to the dephasing and decoherence among the spins, due to which a significant number of spins could go to the subradiant states.

We have seen the evidence that superradiance can be observed with the diamond NV centers. In the next chapters, we'll see the proposal to use the Dicke states prepared during the superradiant emission for magnetometry purposes along with pulsed experiments.

Chapter 3

NV Sample Characterization and Field Detection Experimental Techniques

For the magnetometry and information processing purposes, we first need to characterize the sample, for which we make use of a few experimental techniques, such as, Rabi oscillation, Ramsey sequence, and Hahn Echo sequence, which give us information about the π pulse, T_2^*, and T_2 of the system. A π pulse gives the information about the pulse that is required to transfer the population from spin $m_s = 0$ state to $m_s = \pm 1$ state. T_2, or coherence time, or spin-spin relaxation time, is the time constant of the sample that is related to the continuous dephasing of spinning dipoles that results in decay in the transverse plane magnetization. T_2^* is like T_2, but this decay time also takes into account the heterogeneous inhomogeneities in the surrounding magnetic field of the spins. So, T_2^* or dephasing time is effective T_2 that limits most of our sensing and information processing experiments [Suter 17]. In advanced experiments for sensing and information processing, we make use of dynamical decoupling techniques, that increase the effective dephasing time close to coherence time T_2 [Doherty 13]. There's another fundamental relaxation time, T_1 relaxation time or spin lattice relaxation time, that is the measure of how long the spins are going to be polarized once polarized to $m_s = 0$ state before it start to relax via diamond lattice to $m_s = \pm 1$ state [Suter 17]. In this chapter, we will see show how to perform these experiments in the laboratory. First, we give a short introduction to the experimental setup at LQNO.

3.1 The Setup

The setup has been built in EPFL by Hossein Babashah, a PhD student at LQNO. It can perform two types of experiments on the NV samples, namely, continuous-wave experiments and pulsed experiments. The continuous wave experiments include optically detected magnetic resonance (ODMR). The pulse experiments that are now working in the setup consist of longitudinal relaxation time T_1, Rabi oscillation, Ramsey, and Hahn Echo measurements.

Additionally, another setup is there which can perform the same type of experiment with a diamond that is glued to the fiber. This technique can have useful application in sensing magnetic fields with a high dynamical range (1 mT to 1T) in challenging environments. The goal of the methods was to increase the photon collection efficiency of the diamond or to find a better method to manipulate the spins inside the diamond more efficiently. To manipulate the spin efficiently, we have a micro-strip antenna with double resonance and a microwave cavity near the NV resonances.

The main experimental setup is fixed and consists of a confocal microscope (100x oil immersion), equipped with a piezo-electric stage, an avalanche photodiode, a single photon counter, a spectrometer, and a cobalt laser at 517 nm which is depicted in Figure 3.1. For the microwave excitation part of the setup, a Rhode and Schwarz SMF100A with a microwave resonator is used. The diamond sample is excited with a green laser and the fluorescence is reflected through a dichroic mirror and detected in the photon counter.
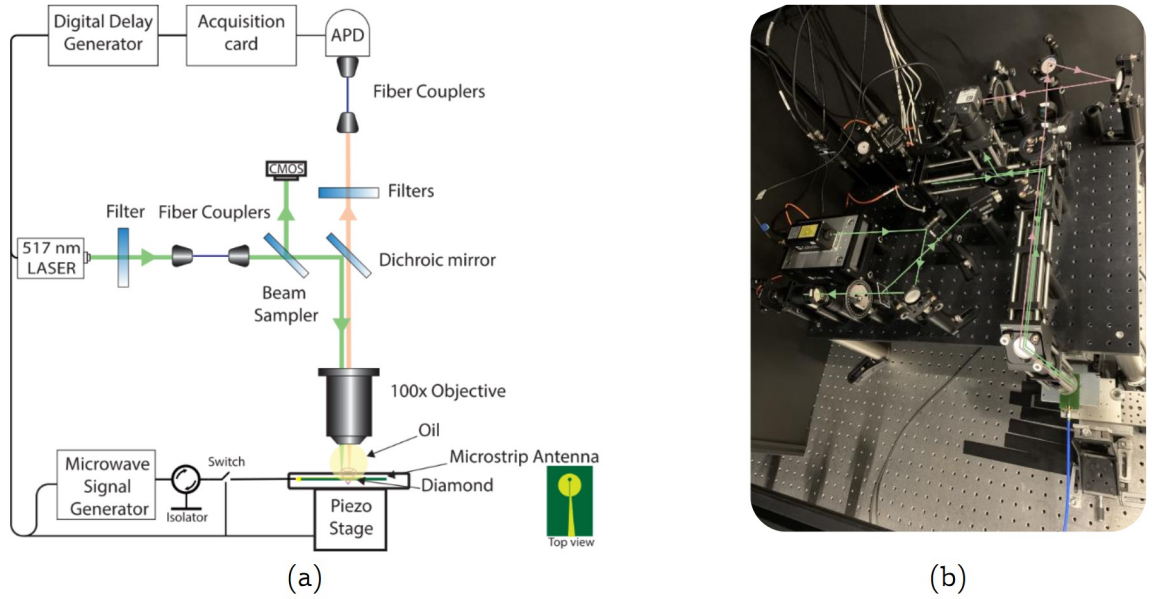
Figure 3.1: (a) The schematic of the setup (b) picture of the setup at LQNO

The complete system is controlled and automized with our python platform called NVLQNO and another platform called Qudi. NVLQNO platform will be available online on Github in the near future. Many efforts and investigations have been devoted to the software development of the platform to fix issues such as laser stabilization and pulse acquisition signal processing. For the first issue of laser stabilization, the power of the laser is readout continuously and then it is used to normalized the output fluorescence. The latter problem of pulse acquisition signal processing is solved by defining several time windows that can go around a certain threshold in a pulse and then find the optimum value for the maximum contrast in the pulse experiments. Furthermore, a method that uses the rising edge of the pulses is applied to further enhance accuracy.

To generate short and complicated pulses, a Swabian pulse streamer is used that is capable to apply any type of complex pulse sequence such as Hahn echo. To apply short pulses that are needed to characterize the samples with

high NV concentration, the SMK-21 module is added to the microwave signal generator. This module is capable to apply microwave pulses within the order of 1 ns needed to measure Hahn Echo. To see the effect of such narrow pulses, a microwave amplifier has been added to the setup that can amplify power up to 48 dBm.

With the setup, optically detected magnetic resonance (ODMR), procedure explained in section 3.2, can be obtained by observing the fluorescence coming from the NV centers inside the diamond while a microwave frequency signal is sweeping between the upper and lower band of spectrum. In Figure 3.2, the stated ODMR is measured and plotted for different microwave powers. One can observe that by increasing the microwave power from -17 dBm to 35 dBm, a saturation has occurred and the spins at $m_s = \pm 1$ are now non-degenerate. This ODMR is measure in the zero-field and the reason for the splitting of the mentioned spins is due to strain present inside the sample.
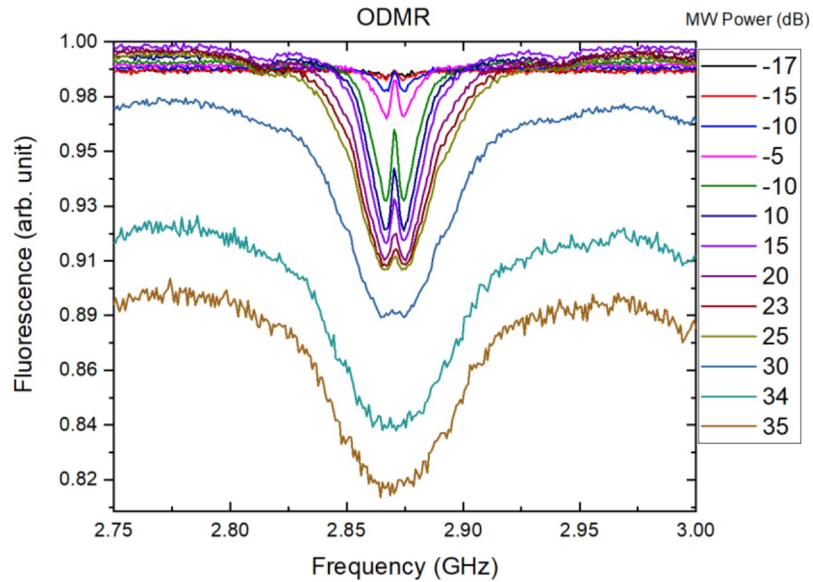
Figure 3.2: ODMR at different microwave power using a microwave amplifier, the broadening of the ODMR dips with increasing power is called power broadening.

In Figure 3.3, measure Rabi oscillations (procedure explained in section 3.3) for

different microwave power is plotted. This measurement is achieved by applying two laser pulses and a microwave pulse in between where the duration of the microwave pulse is changed. sample and its corresponding full width half maximum ODMR dip.
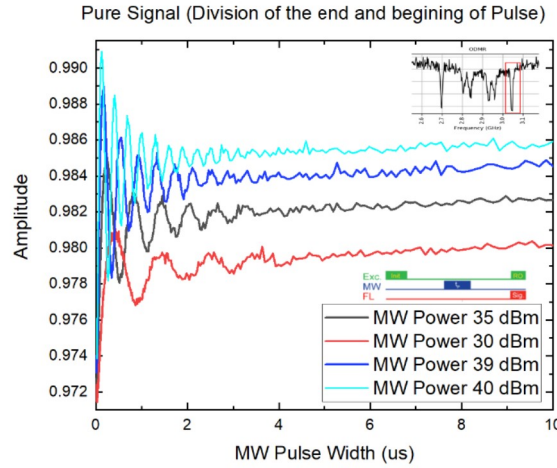
Figure 3.3: Rabi oscillation at different microwave power, with increasing microwave power, the frequency of Rabi oscillations increases [Doherty 13].

Finally, yet importantly, a recent addition was a cleaved fiber to a piece of diamond and then apply all of the measurements that were previously discussed. The schematic and the measurement result of such magnetometer is plotted in Figure 3.4. This so-called fiber-based diamond sensor can have a lot of application in measuring weak magnetic fields with a wide dynamical range from 1 mT to 1 T. Such a compact design can be further enhanced by taking advantage of the geometry of the diamond and improving the way that the fiber is coupled to the diamond. Ideas such as coating the diamond with silver can also be applied to further enhance the sensitivity of this magnetometer.
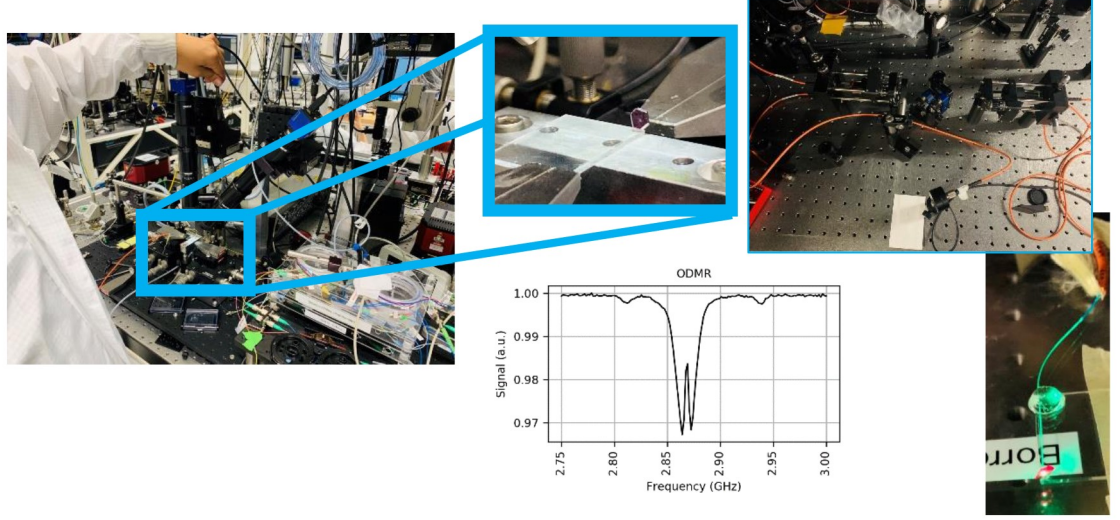
Figure 3.4: Fiber couple experimental setup and the corresponding ODMR

This section was about the details of the setup at LQNO, in the next sections, we explain the experimental procedures and importance of some essential experiments done with the setup. For characterizing any NV sample, we do ODMR, Rabi, T_1, Ramsey sequence, and Hahn Echo experiments, in the similar order. ODMR and Ramsey sequence experiments are also used for magnetometry purposes.

3.2 ODMR

As we discussed in section 2.6, optically detected magnetic resonance (ODMR) in the NV centers is due to the Zeeman effect caused by an external magnetic field on the electronic structure of the defect center [Suter 17].

The figure 3.5 shows the pulse sequence for having the ODMR readings. The green laser is used for state preparation and the state readout [Barry 20a]. When the system is in the $m_s = 0$ state, the fluorescence is brighter as compared

to the $m_s = \pm 1$ states. As the energy difference between the two states is in the GHz range, we sweep the microwave frequency around the zero field splitting of the NV system [Suter 17]. This dip in the contrast of the fluorescence while sweeping the microwave frequencies gives us the resonance frequencies in ODMR.

However, we have worked with the samples containing an ensemble of the NV centers. In the ensemble samples, we have NV axis pointing in all four possible crystallographic orientations [111] [Barry 20a], as shown in figure 3.6.
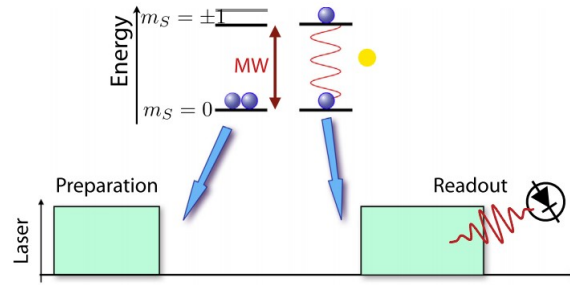
Figure 3.5: The figure shows the pulse sequence for taking the ODMR readings, taken from [Suter 17]. The laser and microwave pulses are applied continuously and simultaneously for ODMR, that's why it is also called a continuous wave (CW) experiment.
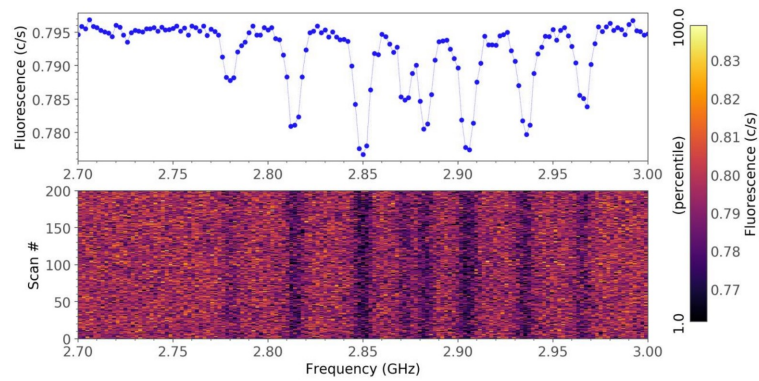
Figure 3.6: Splitting of the ODMR lines corresponding to the four different orientations of the NV axis, each orientation is split into two lines. In the upper portion of the figure, the Y-axis is the normalized fluorescence, and X-axis is the swept frequency. The lower part of the figure shows the number of scans on the Y-axis, and the fluorescence color (as shown in the color bar on right) corresponding to the swept frequency on X-axis.

When we apply an external magnetic field, the projection of the magnetic field on the four orientations is different [Doherty 13], that gives rise to the four different splittings. Our experiment done on the setup shows the four different splittings clearly, as shown in the figure 3.6. The extent of the splitting is according to the Zeeman splitting, $2\gamma_e B_z$, where γ_e is the gyromagnetic ratio and B_z is the magnetic field along the crystallographic orientation, as we saw in section 2.6, making ODMR a way of detecting external magnetic field. We choose one of the ODMR dips from figure 3.6 for further experiments like Rabi oscillations.

3.2.1 Hyperfine Splitting in ODMR

In case of the ensemble samples, we shall have four different electron spin splitting, and each of these would give rise to the hyperfine splitting due to the interaction with the Nitrogen nuclear spin of the NV center, as we saw in section 2.6.1.
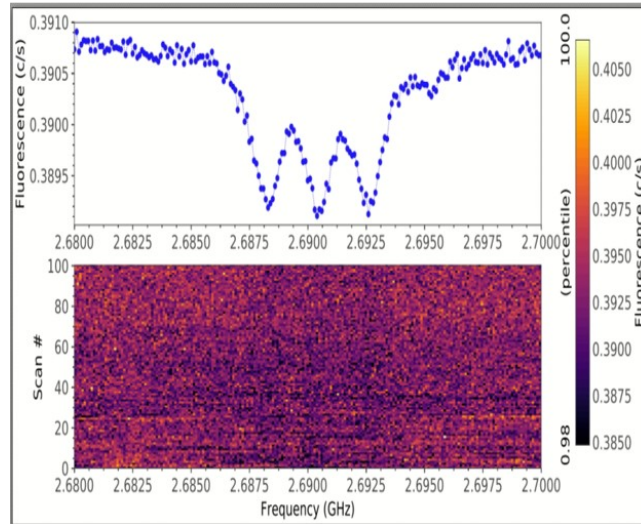
Figure 3.7: The hyperfine splitting of the resonance peak centered near 2.69GHz with a low density NV sample.

The figure 3.7 shows the hyperfine splitting of only one of the four ODMR

dips, the rest three have the similar splittings. For magnetometry applications, we do not always need to work with the hyperfine splittings, however, targeting only one of the dips in the hyperfine ODMR would give us an exact value of microwave frequency to target to for a advanced pulsed experiments like Rabi oscillations, Ramsey and Hahn echo sequences. Nevertheless, we go ahead with one of the ODMR splittings as in figure 3.6 for Rabi oscillations experiment.

3.3   Rabi Oscillations

When we apply a small magnetic field, the ground state $m_s = 0$ and $m_s = 1$ spin transition act as effective two level system [Suter 17]. Applying resonant microwave to drive this transition would cause the population between these two levels to oscillate, also known as Rabi nutations or Rabi oscillations. Measuring the Rabi oscillations is the most basic experiment to be done on an NV sample. It tells us the probability of population transfer between the two energy levels in a two level system [Rondin 14]. For measuring these oscillations, we need to select one of the resonance dips of the ODMR, which is at a particular value of the Microwave(MW) frequency.
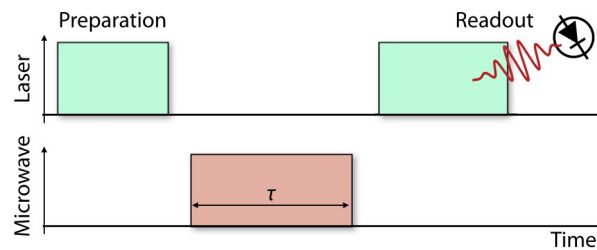
Figure 3.8: The sequence used to measure the Rabi oscillations, the figure is taken from [Suter 17]

The green laser is used to prepare the state, and the selected Microwave frequency is applied for the increasing time duration of the MW radiation. After

such a microwave pulse, another laser pulse is applied to readout the quantum state of the system, as shown in figure 3.8. A similar measurement at 2.74 GHz frequency on LQNO's setup is given in figure 3.9
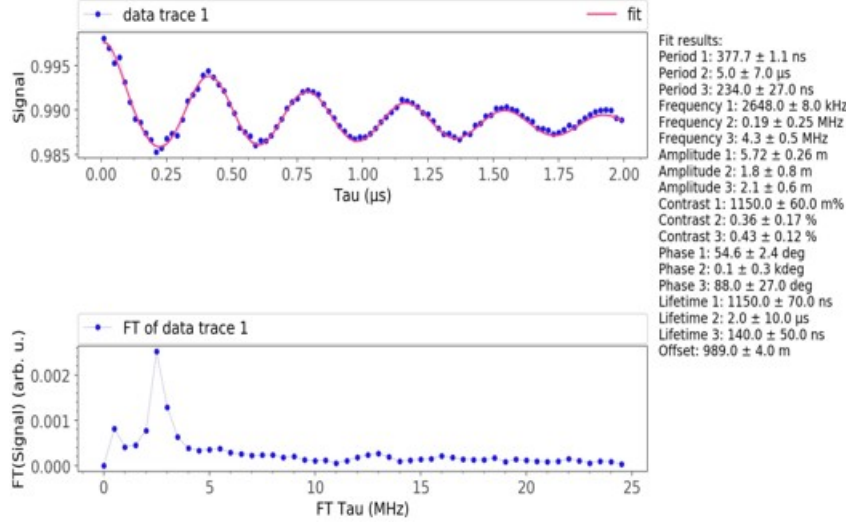
Figure 3.9: The Rabi Oscillations with a highly dense sample. On the right side, there are fit parameters, and the below figure shows the fourier transform of the signal. The Rabi period is 377 ns and a lifetime of 1.15 μs.

In figure 3.9, along with the Rabi oscillations, we also have the Fourier transform of the signal. It has a dominating frequency at 2.65 MHz, and at the right side, we see the dominating time period of 377 ns and has a lifetime of 1.15 μs. One half of the Rabi period gives the π pulse, that we will use for generating Ramsey sequence and Hahn Echo sequences. Before that, we see how to take the readings for the spin-lattice relaxation time T_1.

3.4 Spin-lattice Relaxation: T_1

With T_1, we observe for how long the spins will be staying polarized once the polarization is applied via laser [Jarmola 15]. To check this, we apply a polarizing pulse, wait for some time, and then apply a readout pulse. The

polarizing pulse and the readout pulse, both have the optimum duration of a 100 μs.
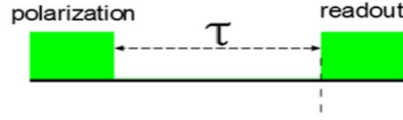
Figure 3.10: Pulse sequence for T$_1$ measurements, the figure is taken from [Jarmola 15]

In figure 3.10, the free duration between the two pulses is swept from a few nanoseconds to a few milliseconds.
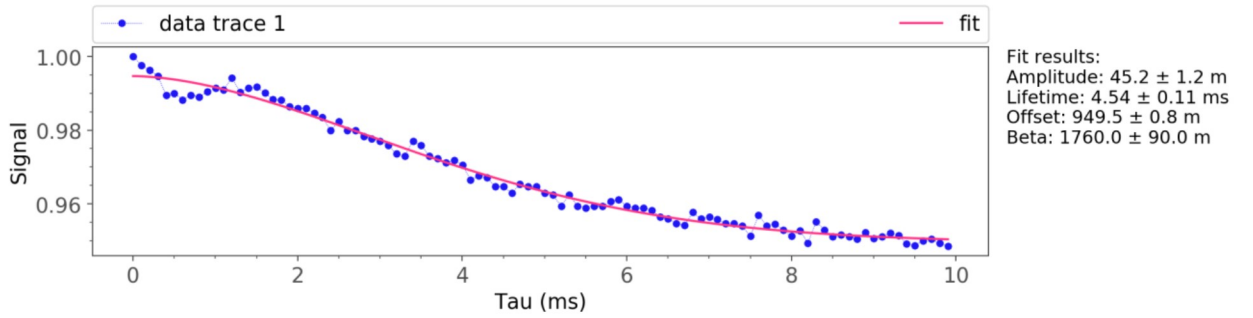
Figure 3.11: Measurement of T$_1$ on a low NV density sample, with a lifetime of 4.54 ms.

The typical T$_1$ values are in milliseconds as shown in figure 3.11, the lifetime is 4.54 ms. This experiment doesn't make use of any microwave pulse and only uses the laser pulses. T_1 is the longest fundamental characteristic time of an NV sample, and T_2^*, T_2 are always less than T_1 [Suter 17], that's what makes the knowledge of T_1 crucial for characterizing an NV sample.

3.5   Ramsey Oscillations: measuring T_2^* and DC magnetic field

The Ramsey sequence measurements gives us the information about the two important things in the magnetometry and information processing: spin dephasing time T_2^*, and the external magnetic field. The pulse sequence for this measurement includes the polarizing laser pulses followed by a microwave $\pi/2$ pulse obtained from the Rabi oscillations. The system is allowed to evolve freely for time τ that is swept, followed by another $\pi/2$ pulse, and then the readout laser pulse.
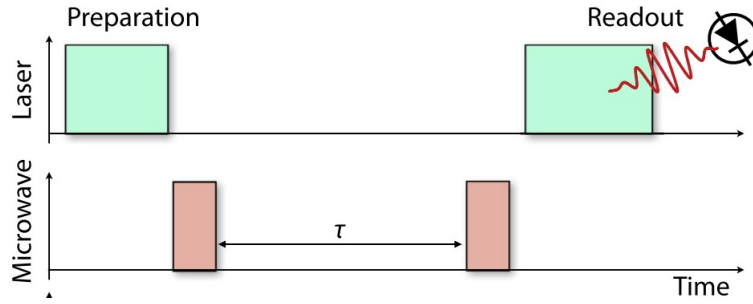
Figure 3.12: Ramsey pulse sequence, the figure is taken from [Suter 17]

As shown in figure 3.12, the time τ between the two microwave pulses is swept from small values to larger values.
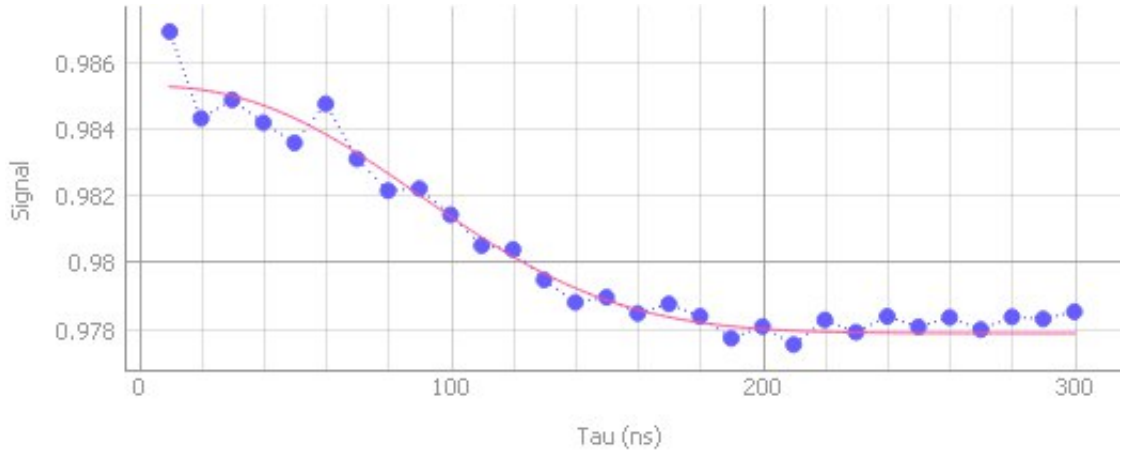
Figure 3.13: Ramsey measurement performed on a dense NV sample. The lifetime is 113 ns.

After Polarization, the first $\pi/2$ pulse would send put the spins to the equator on the Bloch sphere. The free time of evolution would help the states to acquire a phase, that can be made visible by the action of another $\pi/2$ pulse, is read out by another laser pulse [Barry 20a].
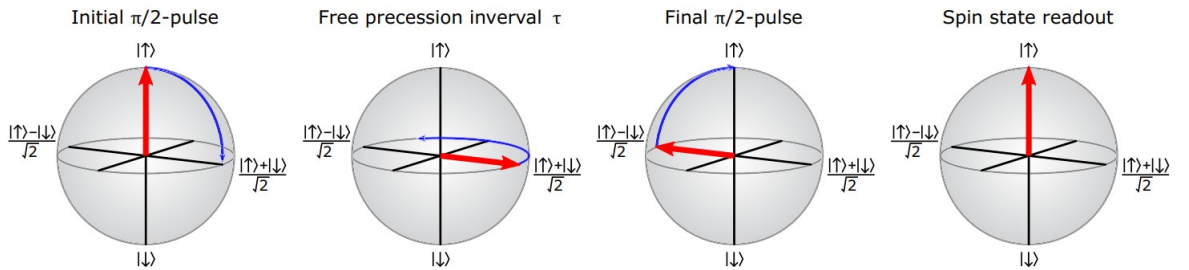
Figure 3.14: Evolution of the system during the Ramsey sequence depicted on a Bloch sphere. The figure is taken from [Barry 20a]

The evolution in figure 3.14 is also helpful in explaining the dephasing time T_2^*. During the step of free evolution between the two $\pi/2$ pulses, the system can go under dephasing. This ways, when we apply the second $\pi/2$ pulse, all of the spins do not point in the same direction, so the fluorescence reduces. With increasing time of the free evolution, the readout fluorescence keeps decreasing exponentially as shown in figure 3.13.

Ramsey sequence is also a way to estimate an external DC magnetic field [Barry 20b],

$$B_{sense} \approx \frac{2}{\hbar \gamma_e \tau} < S_z >$$ (3.1)

where, B_{sense} is the external DC magnetic field, $\hbar$ is the reduced Planck's constant, γ_e is the gyromagnetic ratio, τ is the free evolution time between the two $\pi/2$ microwave pulses, and $< S_z >$ is the reading of NV population made directly from the setup. This way, we can estimate an external DC magnetic field with Ramsey sequence in the lab. In the next section, we will seen Hahn Echo technique to increase the effective dephasing time using a decoupling π pulse in between the Ramsey sequence.

3.6 Hahn Echo: measuring $\sim$ T$_2$

Hahn Echo sequence is the most basic decoupling sequence used in the information processing and in magnetometry [Rondin 14], whose lifetime is close to the T_2 or the coherence time of the system. In the Hahn Echo sequence, along with the two $\pi/2$ pulses as was in Ramsey, we also have another π pulse in between the two $\pi/2$ pulses as show in figure 3.15.
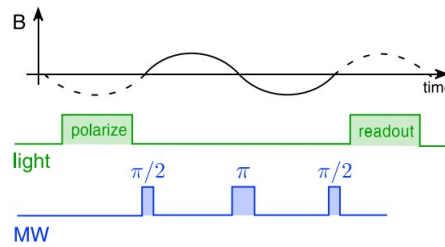
Figure 3.15: The Hahn Echo pulse sequence (adapted from [Rondin 14])

The additional π pulse would recombine the dephasing spins and would help keep the system remain in phase for additional time. The readout laser's fluorescence decreases exponentially with time.
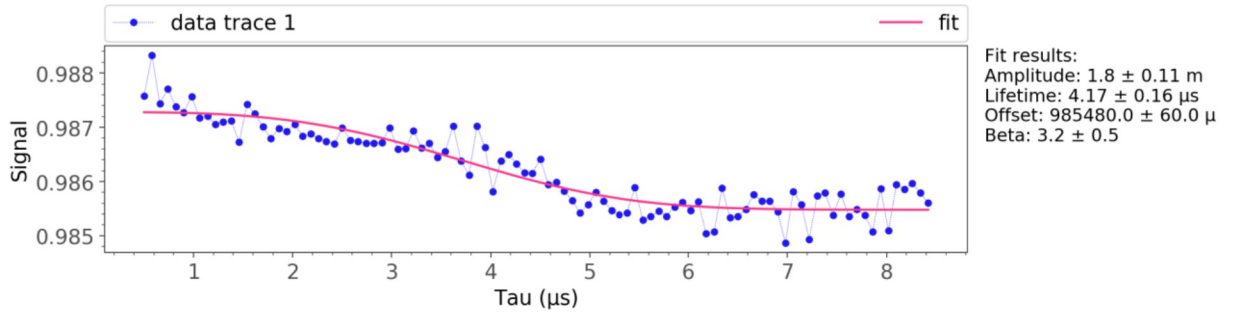
Figure 3.16: The Hahn Echo measurement on a low density sample, T_2 is nearly 4.17 μs.

As shown in figure 3.16, the lifetime of the decay is 4.17 μs, that is at least an order of magnitude more than the Ramsey sequence, thanks to the additional π pulse between the two $\pi/2$ pulses. The process of recombination of the spins can be also understood with the Bloch sphere.
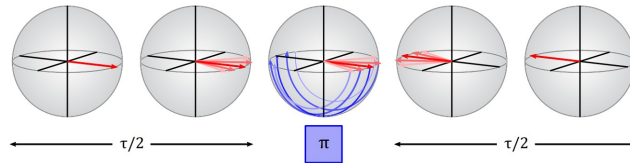
Figure 3.17: The depiction of the Hahn Echo evolution on the Bloch sphere. The figure is taken from [Barry 20a]

As shown in figure 3.17, the π pulse applied would compensate for the spins dephasing because of the field inhomogeneities (characterized by T_2^*). The π pulse would try to cancel the T_2^* dephasing, it also makes the system insensitive to the static field signals. The new time scale is close to the decoherence time T_2.

With the experiments discussed above, we can fully characterize an NV sample.

Next, we see the limitations of the experimental DC magnetic field detection techniques that we already discussed in sections 3.2 and 3.5 with ODMR and Ramsey sequence respectively.

3.7 Sensitivity limitations to current schemes

Generally, the sensitivity for the measurement of a magnetic field is given by,

$$B_{min} = \frac{\sigma(t)}{\frac{dS}{dB}} \tag{3.2}$$

The system's signal standard deviation $\sigma(t)$ is checked with the response of the signal dS with change in the magnetic field dB. For NV centers using a pulsed detection scheme, the sensitivity is given by, [Neumann 15]

$$B_{min}(t) = \frac{\sigma_1}{\gamma A T_\phi \sqrt{n}} \tag{3.3}$$

Here, $n = \frac{t}{T_{seq}}$ with t as total measurement time. T_{seq}, σ_1, and T_ϕ are the duration, standard deviation, and the phase accumulation time of a single field evaluation. A is the system-specific amplitude of the signal modulation. For independent emitters, σ_1 should scale as the spin projection noise $\frac{1}{\sqrt{N}}$, where N is the number of NV spins. This is the case for the DC magnetic field detection with ODMR and Ramsey sequence in sections 3.2 and 3.5 respectively, where magnetic field sensing is with the non-entangled independent emitters. This way, sensitivity is limited by the standard quantum limit (SQL) or $\frac{1}{\sqrt{N}}$ standard deviation limit of sensing. The minimum magnetic field observed with

these schemes is given by the expression,

$$B_{min-non-entangled} = \frac{1}{\gamma \sqrt{\frac{Nt}{T_{seq}}} T_\phi \exp\left\{-\frac{T_{phi}}{T_2}\right\}} \qquad (3.4)$$

However, if we were having NV system in an entangled states as a Dicke state, we would have σ_1 given by $\frac{\sqrt{2}}{\sqrt{N(N+2)}}$ [Apellaniz 15], also known as the Heisenberg limit. Which is $\frac{\sqrt{2}}{\sqrt{N+2}}$ times less than the shot noise limit of $\frac{1}{\sqrt{N}}$ standard deviation. Hence, a sensor working under Heisenberg limit is way more sensitive than the independent emitters having SQL. In the next chapter, we shall see the use of superradiance to prepare such a Dicke state [Dicke 54] and will propose it's use for magnetic field sensing with NV centers.

Chapter 4

Proposal: Sensing with Dicke states

As we saw in the last chapter, the typical sensing techniques are limited by the standard quantum limit (SQL), and a more field sensitive alternative is the use of entanglement for magnetic field sensing [Apellaniz 15], that is bound by more sensitive Hesinberg limit. Building upon the phenomenon of superradiance discussed in section 2.7, in this chapter, we will explain the idea of making use of superradiance for preparing the highly entangled Dicke states, that would have significant advantage in magnetic field sensing over non-entangled states.

4.1 Preparation of the Symmetric Dicke state: Detuning the cavity

During superradiant emission, the collective state of the NV spins goes through a ladder of highly entangled states called the Dicke states [Dicke 54] as shown in figure 4.1. As the system goes down the Dicke ladder, when the value of magnetic quantum number is $|0\rangle$, we have the most entangled Dicke state, and at that point, we have the hump in the superradiant emission profile (figure 2.7) and the intensity is proportional to N^2.
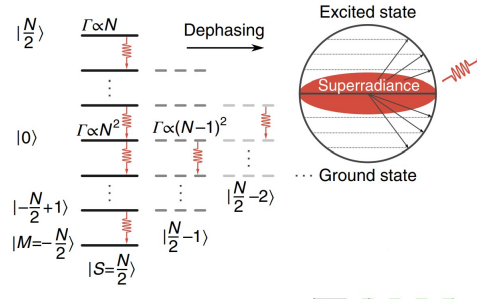
Figure 4.1: The Dicke ladder the NV system goes through during a superradiant emission (adapted from [Angerer 18]). The generalized Bloch sphere shows the equator in red where the most entangled Dicke states is achieved. At that moment, the emission profile follows N^2 proportionality, a property of superradiant emission.

We have seen in section 2.7 we need a microwave resonator for having the superradiant emission from the diamond NV centers. The characteristic frequency of the cavity is matched with that of the NV centers for having the superradiant emission. We propose to detune the cavity's frequency in the mid of the superradiant emission, when the quantum state of the NV system is moving down the Dicke ladder close to $|0\rangle$ state in figure 4.1. The detuning of the cavity could be done with the use of a switch at the pre-calculated delay time of the superradiant emission (figure 4.2).
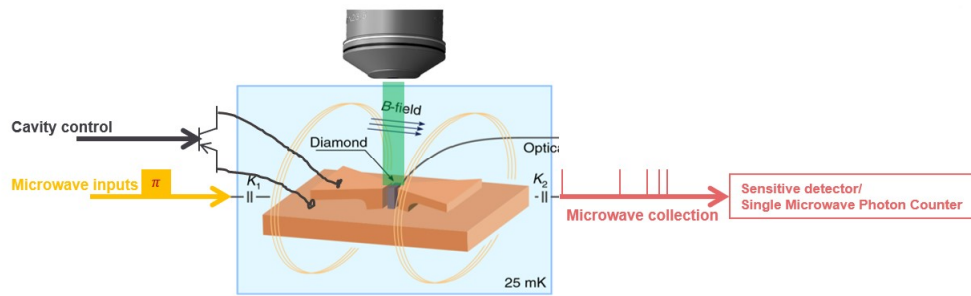
Figure 4.2: The scheme for opening the cavity inspired from [Angerer 18]. First, the polarization is done with the green laser, and a π pulse is sent for the population inversion. Then the superradiant emission profile is recorded with the microwave detector. Further, with the help of the cavity control, the cavity is detuned from the initial frequency at the estimated time of the hump of the superradiant emission, as in figure 2.7. This way, we have highly entangled Dicke states prepared with us that we use for magnetic field sensing.

Delay time is the characteristic time of the superradiant emission that determines the lifetime of the emission profile [Shammah 17]. As the delay time is quite crucial in deciding when to detune the cavity, we check how the delay time changes with opening the cavity by detuning. The delay time of the superradiant emission is given by [Shammah 17],

$$t'_d = \frac{ln(N)}{N\gamma'_s} \tag{4.1}$$

where N is the total number of spins in the system and γ'_s is the spontaneous emission rate when inside the cavity. γ'_s, the emission rate, is affected by the Purcell factor of the cavity, F_P, and $\gamma'_s = \gamma_s \times F_P$ [wik].

When the system is opened, that is, the cavity is detuned, the emission is the typical spontaneous emission, for which, the delay time is

$$t_d = \frac{ln(N)}{N\gamma_s} \tag{4.2}$$

We expect that $t_d >> t'_d$, as F_P is supposed to be quite high in our case (we estimated it to be close to 34,000 in section 2.8.2). Hence, there is going to be a time difference of close to 34,000 times in the delay time before and after detuning the cavity. The delay time after detuning the cavity will be longer as compared to before opening the cavity.

When we open the system, that is, we decouple the cavity from the diamond NV center ensemble at superradiant time delay t_d, we expect the NV center ensemble in the most entangled Dicke state. A Dicke state is given by,

$$|D_N^m\rangle = \binom{N}{m}^{-\frac{1}{2}} \sum_k \mathscr{P}_k(|1\rangle^{\otimes m} \otimes |0\rangle^{\otimes(N-m)}) \tag{4.3}$$

and the most entangled Dicke state is for even N and $m = \frac{N}{2}$. We denote it by $|D_N\rangle$, given by,

$$|D_N\rangle = \left| D_N^{\frac{N}{2}} \right\rangle \tag{4.4}$$

The state we get in equation 4.4 is the one that we will analyze for magnetic field detection. Now, we simulate the system of 20 spins for the emission profile before and after opening the cavity.

Simulation results We took N = 20, and had simulated the superradiance emission for two different environments of the spin system, first when there is cavity, and the second one when we open the cavity. In the first case, the spontaneous emission rate is enhanced by ≈ 34000 due to the cavity (the Purcell factor). We use QuTip [Johansson 12] to simulate the result in fig 4.3 and fig 4.4.
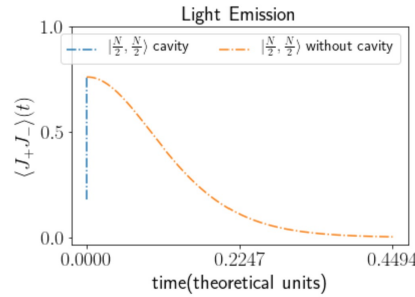
Figure 4.3: The emission pattern before and after opening the cavity, the blue curve corresponds to the emission within the cavity, while the other one is for after we open the cavity. Y-axis shows the normalized intensity of emission, and X-axis shows the time in theoretical/dummy units.
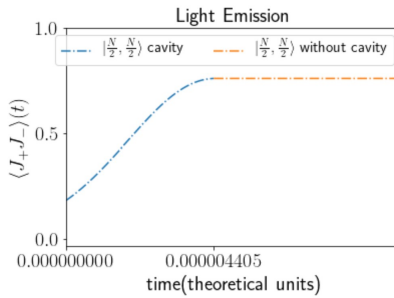
Figure 4.4: Zoomed in view of figure 4.3

As shown in figures 4.3, for the system within the cavity, the delay time is far less than while without the cavity. We have got this result by solving the kind of the master equation given in equation 2.3, which takes care of the dynamics of the system. Figure 4.5 shows the emission profile when procedure of opening the cavity and having the Dicke states prepared is applied.
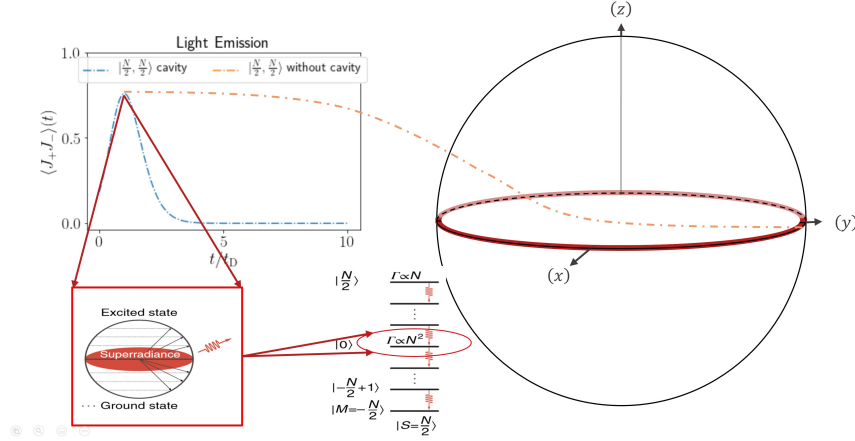
Figure 4.5: Emission and Quantum state profile as we open the cavity. The Bloch sphere on the right shows the expected quantum state, that would be near the equator (the sphere on the down shows the same thing). At the time we open the cavity, the ladder below shows that the emission profile is proportional to N^2 and is at the time of the hump in the emission profile of the superradiant emission. Opening the cavity would delay the emission time (orange) of emission profile, and we would have states close to the equator intact for a considerably longer time.

Once we have the dicke state, we can do the measurement of the Dicke state with dispersive technique [Astner 18] . In the next section, we see how to use the most entangled Dicke state for the magnetic field detection.

4.2   Magnetic field sensing with Dicke state

For a Dicke state given in equation 4.4, J_z^2 is the optimal operator to measure for the ideal Dicke state for metrology, and the inverse of the precision is given

by [Apellaniz 15],

$$(\Delta\theta)^2_{opt} = \frac{2}{N(N+2)} \tag{4.5}$$

where, θ is the parameter must be estimated based on measuring an observable on the final state. Equation 4.5 means that higher the number of the spins N, higher is the precision.

After the cavity is opened, the system remains with the ensemble of NV centers Hamiltonian [Barry 20b], which can be written as,

$$H = \sum_{n=1}^{N} (2\pi D + \gamma_e(\vec{B}.\vec{S}_n)) \tag{4.6}$$

We use the Ramsey sequence discussed in 3.5 for the magnetic field detection with the Dicke state, as shown in figure 4.6.

Figure 4.6: Ramsey sequence used for magnetic field detection with a Dicke state. The free evolution time gets the information of the external magnetic field.

When we apply the ramsey sequence on our prepared Dicke state, as shown in figure 4.7, which is at the equator of the giant Bloch sphere, the first $\pi/2$ pulse would rotate the state to the vertical axis of the Bloch sphere. The free

evolution time provides the state time to interact with the external magnetic field to be sensed, and the state is rotated around Z axis of the Bloch sphere. The last $\pi/2$ rotation would allow the measurement and the calculation of the J_z^2 on the NV system.
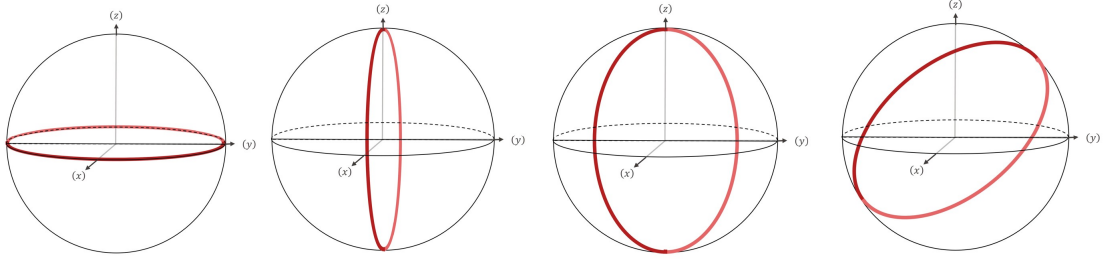
Figure 4.7: Evolution of the prepared Dicke state with the application of Ramsey sequence.

Also, any off-axis magnetic field component $B_\perp$ can be ignored as long as $\frac{(\gamma_e B_\perp)^2}{[(2\pi D)^2 \pm (\gamma_e B_0)^2]} << 1$, where $D = 2.87 GHz$ is the zero-field splitting and $\gamma_e = g_e \mu_B / \hbar$ is the gyromagnetic ratio of the NV^- electron spin. The system can be described by a pseudo spin-$\frac{1}{2}$ Hamiltonian,

$$H = \sum_{n=1}^{N} (2\pi D + \gamma_e B) S_{z,n} \tag{4.7}$$

here, $S_z = \frac{\hbar}{2} \sigma_z$, and $B = B_0 + B_{sense}$. This Hamiltonian would be used for detecting the Magnetic field. Also, for reading out from a Dicke state, we need to make a measurement of the J_z^2 operator [Apellaniz 15]. In practice, we shall make the same projective measurement on J_z, but instead of taking the average of the data, we need to calculate the variance at each point in time for the Ramsey sequence.

As we saw in section 3.7, the sensitivity for the measurement of a magnetic field is given by,

$$B_{min} = \frac{\sigma(t)}{\frac{dS}{dB}} \tag{4.8}$$

In this method to calculate the sensitivity, the system's signal standard deviation $\sigma(t)$ is checked with the response of the signal dS with change in the magnetic field dB. For NV centers using a pulsed detection scheme, the sensitivity is given by, [Neumann 15]

$$B_{min}(t) = \frac{\sigma_1}{\gamma A T_\phi \sqrt{n}} \tag{4.9}$$

Here, $n = \frac{t}{T_{seq}}$ with t as total measurement time. T_{seq}, σ_1, and T_ϕ are the duration, standard deviation, and the phase accumulation time of a single field evaluation. A is the system-specific amplitude of the signal modulation. For independent emitters, σ_1 should scale as the spin projection noise $\frac{1}{\sqrt{N}}$, where N is the number of NV spins. However, for the collective emitters we have σ_1 given by $\frac{\sqrt{2}}{\sqrt{N(N+2)}}$ [Apellaniz 15]. Finally, the sensitivity with the Dicke state would be given by,

$$B_{min-Dicke} = \frac{\sqrt{2}}{\gamma \sqrt{\frac{N(N+2)t}{T_{seq}}} T_\phi \exp\left\{-\frac{T_{phi}}{T_2}\right\}} \tag{4.10}$$

For a case where $T_{seq} \longrightarrow T_\phi$, and the minimum of the equation above would be achieved at $T_\phi = \frac{T_2}{2}$ [Neumann 15], which simplifies the previous equation to,

$$B_{min-Dicke} = \frac{2\sqrt{e}}{\gamma \sqrt{N t T_2}} = 1.84 \times 10^{-11} \; T / \sqrt{N(N+2)t T_2} \tag{4.11}$$

The sensitivity with Dicke states is improved by a factor of almost $\frac{1}{\sqrt{N}}$, reaching the Heisenberg limit of sensing in principle. The current magnetometers have sensitivity upto $10^{-12} T/\sqrt{Hz}$ [Neumann 15], while with our proposal, we can reach upto the sensitivity of $10^{-18} T/\sqrt{Hz}$ for the diamond sample used in the superradiance with NV center experiment [Angerer 18]. Next, we show the simulation in QuTip [Johansson 12] of the Ramsey sequence with Dicke states for 10 spins.

4.3 Modeling 10 spins

To demonstrate the use of Ramsey sequence with Dicke states in the NV canters, we use QuTip to simulate 10 spins evolution under Ramsey sequence after opening the cavity. The magnetic field detection can be done by the Ramsey sequence [Barry 20b]. The analysis of the variance of the readout (J_z^2) of the spin population would give us the information about the external magnetic field. In figure 4.8 we show the simulation results for 10 spins prepared in the transient Dicke state by opening the cavity in the peak of the superradiant emission. The different curves are for two different values of the magnetic fields, the first one is the half of the other, and the difference in the oscillation frequency of the two is visible. The results are generated with QuTip [Johansson 12].
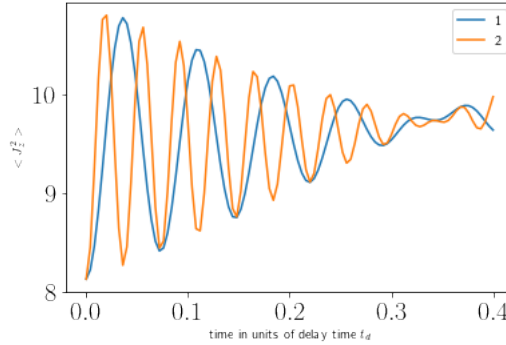
Figure 4.8: A simulation for the Ramsey sequence with the transient Dicke state after opening the cavity, the two colors show the evolution of the state for two different magnetic fields.

4.4 Applications

Our proposal promises sensing close to the Heisenberg limit experimentally with diamond NV centers. As magnetometry with entangled states would give better sensing than the existing magnetometers [Apellaniz 15], it would have direct applications in better sensing and detecting the sub cellular magnetic particles

inside a cell as already demonstrated with the typical magnetometers [Kuwahata 20], consequently having biomedical applications. The other advantages of the advanced sensing would include metrology applications and imaging of neural activities in brain, as demonstrated with typical diamond NV magnetometers [Doherty 14, Karadas 18].

Chapter 5

Further Experiments and Concluding Remarks

For observing superradiance from Diamond NV centers in Microwave regime, we designed a microwave cavity similar to that in section 2.8 in collaboration with Hossein Babashah, a PhD student at LQNO. In this chapter, we report the fabrication and the experiments on the cavity with the NV centers. As it is the latest progress on the project, we conclude this thesis in this chapter.

5.1   Microwave Cavity Fabrication and Experiments

For the experiment, we shall need a low Q cavity acting in the bad cavity regime [Angerer 18]. We can freeze the symmetric Dicke state by opening the cavity in the midst of superradiant emission by changing the fundamental frequency of the cavity with the help of a switch. We simulated a cavity with the same requirements as described above. It is evident from the figure 5.1 that the coupling to the spins is highest at the bow-tie, where the diamond sample shall be placed.
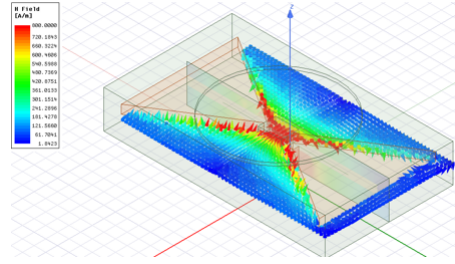
Figure 5.1: A simulation of the microwave cavity with Ansys HFSS to be used for the experimental purpose. The color bar shows the value of magnetic field throughout cavity in simulation.

We designed a microwave resonator to efficiently target all the spins of a bulk diamond with a lot of concentration of NVs and low microwave power. This way, spins can be coupled to a single cavity mode, in order to have enhanced emission for collective emission. In order to have a enhanced coupling to the spins, we need to have bigger microwave field as compared to normal antenna. A 3-D lumped resonator, the cavity we are using for the experiment, has an advantage of having the concentrated magnetic field in the center. We fabricated the above mentioned cavity as shown in figure 5.2.
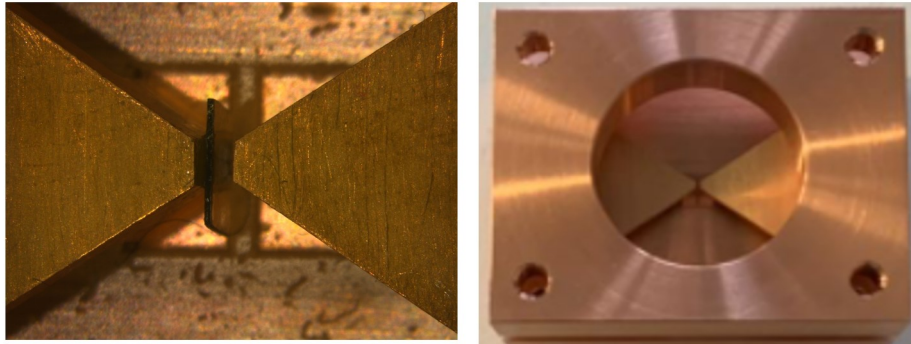
Figure 5.2: The fabricated Microwave cavity, the left is one with the sample, and the right one is the full packed cavity. The cavity has a whole at the top to accommodate the microscope objective for spin initialization and readout.
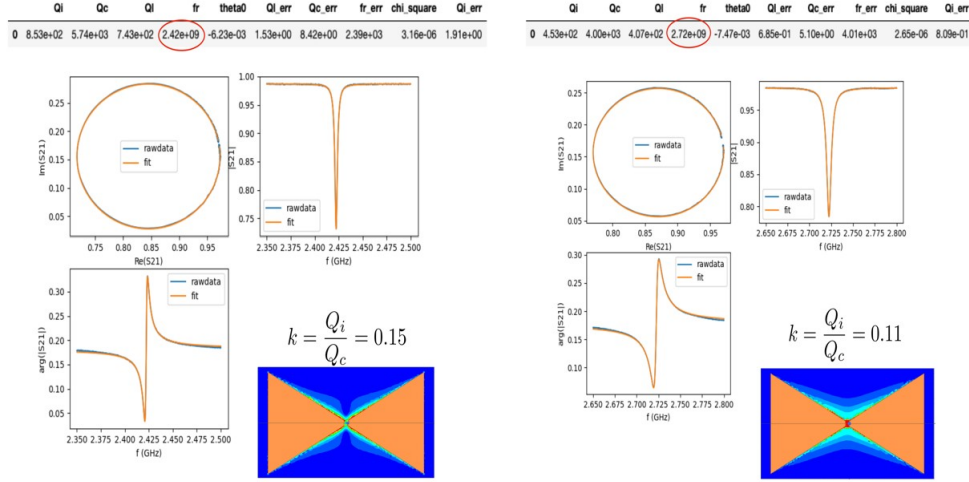
Figure 5.3: Analysis of the cavity signal from a vector network analyzer (VNA). Our cavity has two resonance frequency at 2.42 GHz and 2.72 GHz, the simulation corresponding to both shows that the one of at 2.72 GHz has magnetic field concentrated between the bow-ties. We used the code in [Probst 15] for fitting the cavity measurements from the VNA and got these results. The code takes the output of the VNA and fits it for the value of reflectance of the input signal. The fitted parameter give the fit values for the cavity frequency and effective q-factor.

We used a vector network analyzer (VNA) to characterize the fundamental frequencies and the Q-factor of the cavity that is related to the total losses from the cavity. We used a python code [Probst 15] to fit the signal of the VNA to find the cavity parameters. The cavity has two fundamental frequency, one at 2.42 GHz and another at 2.72 GHz, as shown in figure 5.3, with effective quality factors 743 and 407 respectively that meet our requirement of low quality factor cavity. Currently, we are doing experiments with the cavity on our setup that is shown in figure 5.4.
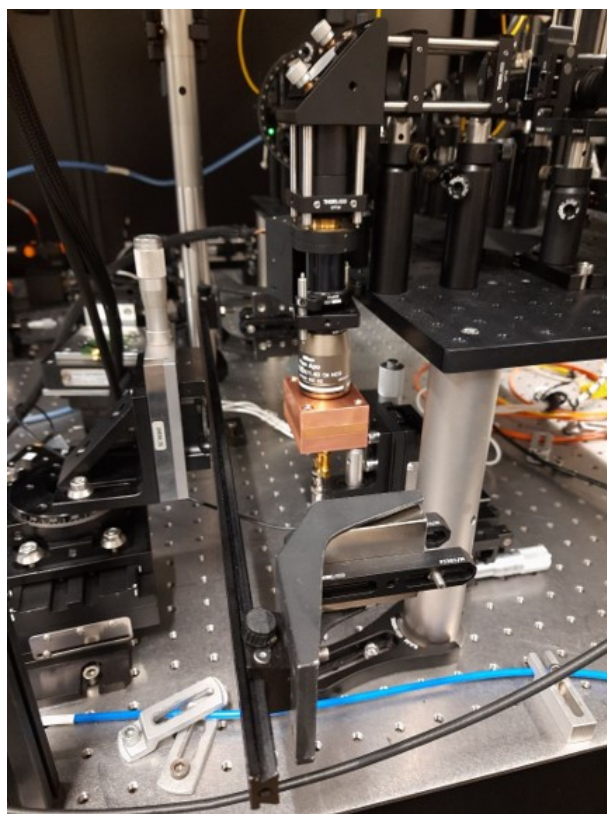
Figure 5.4: Picture of the microwave cavity in the setup during a measurement. The microscope objective on the top of the cavity sends laser to initialize and readout the spin states. The magnets on the stage are used to apply the required magnetic field to match the resonance of the cavity to that of the NV center's.

With the cavity, we have performed the ODMR for bringing the dip to the resonance peak of the cavity, figure 5.5. Then, we have done the Rabi oscillation experiment for getting the π pulse, figure 5.6.
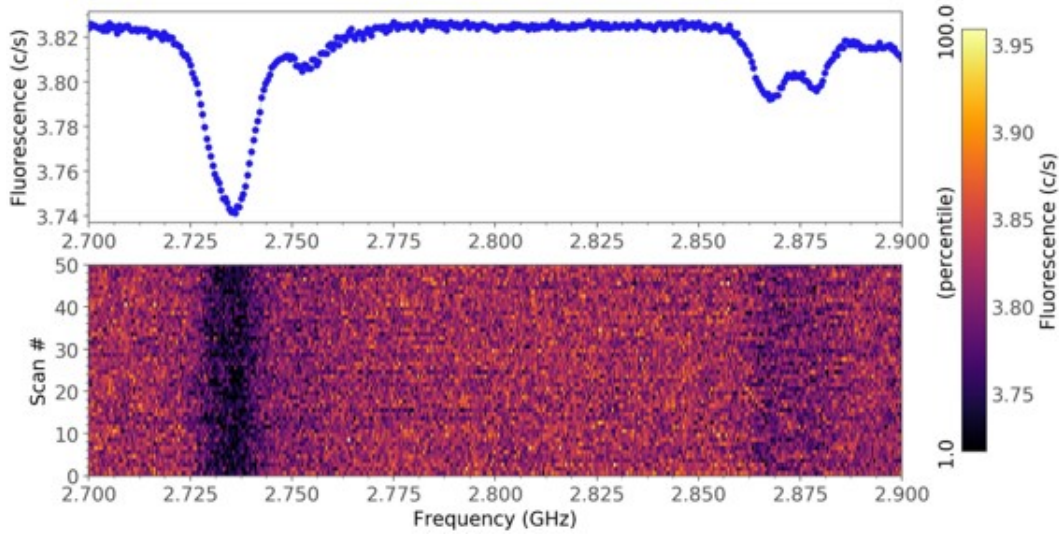
Figure 5.5: Bringing the resonance of the NV center ODMR peak to the one of the resonance of the cavities near 2.72 GHz.
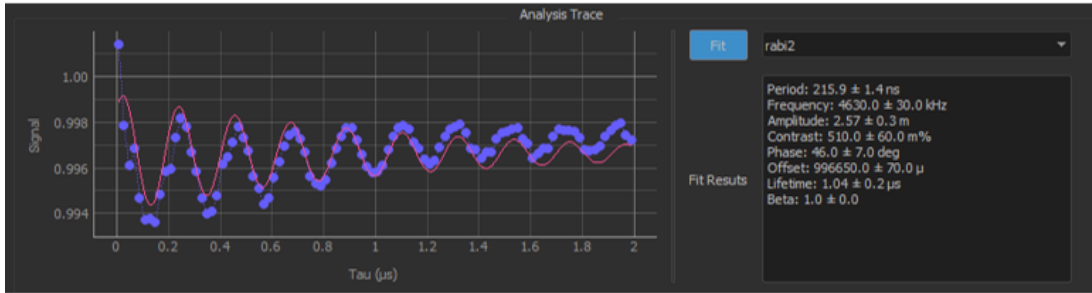
Figure 5.6: Doing the Rabi oscillation experiment at the cavity resonance, Rabi period is 215 ns.

Our current efforts and future plans include observing superradiance with the cavity. The next step would be to prepare the Dicke state and do the sensing experiments as described in the last chapter. The experiments are in progress at LQNO, EPFL.

5.2   Conclusion

In this thesis, we started with an introduction to diamond NV centers and their electronic, optical properties, and superradiance from diamond NV centers in chapter 2. In chapter 3, we reviewed the experimental techniques and for sample characterization and magnetic field sensing with its fundamental standard quantum limit (SQL). We propose a new sensing method reaching the Heisenberg limit with Dicke states achieved during the superradiant emission in chapter 4. We are on the way to realize our scheme experimentally, for that, we have designed the required cavity and have performed basic experiments as ODMR and Rabi with NV centers inside the cavity. The further experiments on the resonator to observer superradiance and implement the scheme are in progress at EPFL.

References

[Angerer 16]   Andreas Angerer, Thomas Astner, Daniel Wirtitsch, Hitoshi Sumiya, Shinobu Onoda, Junichi Isoya, Stefan Putz & Johannes Majer. *Collective strong coupling with homogeneous Rabi frequencies using a 3D lumped element microwave resonator*. Appl. Phys. Lett., vol. 109, page 033508, 2016.

[Angerer 18]   Andreas Angerer, Kirill Streltsov, Thomas Astner, Stefan Putz, Hitoshi Sumiya, Shinobu Onoda, Junichi Isoya, William J. Munro, Kae Nemoto, Jörg Schmiedmayer & Johannes Majer. *Superradiant emission from colour centers in diamond*. Nature Physics, vol. 14, page 1168–1172, 2018.

[Apellaniz 15] Iagoba Apellaniz, Bernd Lücke, Jan Peise, Carsten Klempt & d Géza Tóth. *Detecting metrologically useful entanglement in the vicinity of Dicke states*. New Journal of Physics, vol. 17, page 083027, 2015.

[Aslam 13]   N Aslam, G Waldherr, P Neumann, F Jelezko & J Wrachtrup. *Photo-induced ionization dynamics of the nitrogen vacancy defect in diamond investigated by single-shot charge state detection*. New J. Phys., vol. 15, page 013064, 2013.

[Astner 18]   T. Astner, J. Gugler, A. Angerer, S. Wald, S. Putz, N. J. Mauser, M. Trupke, H. Sumiya, S. Onoda, J. Isoya, J. Schmiedmayer, P. Mohn & J. Majer. Nature Materials, vol. 17, pages 313–317, 2018.

[Barry 20a]   John F. Barry, Jennifer M. Schloss, Erik Bauch, Matthew J. Turner, Connor A. Hart, Linh M. Pham & Ronald L. Walsworth. *Sensitivity optimization for NV-diamond magnetometry*. Rev. Mod. Phys., vol. 92, page 015004, 2020.

[Barry 20b]   John F. Barry, Jennifer M. Schloss, Erik Bauch, Matthew J. Turner, Connor A. Hart, Linh M. Pham & Ronald L. Walsworth. *Sensitivity optimization for NV-diamond magnetometry*. Rev. Mod. Phys, vol. 92, page 015004, 2020.

[Breeze 15]   Jonathan Breeze, Ke-Jie Tan, Benjamin Richards, Juna Sathian, Mark Oxborrow & Neil McN Alford. *Enhanced magnetic Purcell effect inroom-temperature masers*. Nature Communications, vol. 6, page 6215, 2015.

[Chu 15]   Yiwen Chu & Mikhail D. Lukin. *Quantum optics with nitrogen-vacancy centers in diamond*. Oxford University Press, vol. Quantum Optics with Nitrogen Vacancy centers in Diamond, 2015.

[Dicke 54]   R.H. Dicke. *Coherence in Spontaneous Radiation Processes*. Phys. Rev., vol. 93, page 99, 1954.

[Doherty 13]   Marcus W. Doherty, Neil B. Manson, Paul Delaney, Fedor Jelezko, Joerg Wrachtrup & Lloyd C.L. Hollenberg. *The nitrogen-vacancy colour centre in diamond*. Phys. Rep., vol. 1, page 528(1), 2013.

[Doherty 14]   Marcus W. Doherty, Viktor V. Struzhkin, David A. Simpson, Liam P. McGuinness, Yufei Meng, Alastair Stacey, Timothy J. Karle, Russell J. Hemley, Neil B. Manson, Lloyd C.L. Hollenberg & Steven Prawer. *Electronic Properties and Metrology Applications of the Diamond NV- Center under Pressure*. Phys. Rev. Lett., vol. 112, page 047601, 2014.

[Gross 82]   M. Gross & S. Haroche. *Superradiance: an essay on the theory of collective spontaneous emission*. North Holland Publishing Company, 1982.

[Hall 12]   L. T. Hall, G. C. G. Beart, E. A. Thomas, D. A. Simpson, L. P. McGuinness, J. H. Cole, J. H. Manton, R. E. Scholten, F. Jelezko, Jörg Wrachtrup, S. Petrou & L. C. L. Hollenberg. *High spatial and temporal resolution wide-field imaging of neuron activity using quantum NV-diamond*. Scientific Reports, vol. 2, page 401, 2012.

[Jarmola 12]   A. Jarmola, V. M. Acosta, K. Jensen, S. Chemerisov & D. Budker. *Temperature- and Magnetic-Field-Dependent Longitudinal Spin Relaxation in Nitrogen-Vacancy Ensembles in Diamond*. Phys. Rev. Lett., vol. 108, page 197601, 2012.

[Jarmola 15]   A. Jarmola, A. Berzins, J. Smits1, K. Smits, J. Prikulis, F. Gahbauer, R. Ferber1, D. Erts3, M. Auzinsh & D. Budker. *Longitudinal spin-relaxation in nitrogen-vacancy centers in electron irradiated diamond*. Applied Physics Letters, vol. 107, page 242403, 2015.

[Johansson 12]   J. R. Johansson, P. D. Nation & F. Nori. *QuTiP: An open-source Python framework for the dynamics of open quantum systems*. Computer Physics Communications, vol. 183, page 1760, 2012.

[Karadas 18]   Mürsel Karadas, Adam M. Wojciechowski, Alexander Huck, Nils Ole Dalby, Ulrik Lund Andersen & Axel Thielscher. *Feasibility and resolution limits of opto-magnetic imaging of neural network activity in brain slices using color centers in diamond*. Scientific reports, vol. 8, page 4503, 2018.

[Kuwahata 20]   Akihiro Kuwahata, Takahiro Kitaizumi, Kota Saichi, Takumi Sato, Ryuji Igarashi, Takeshi Ohshima, Yuta Masuyama,

Takayuki Iwasaki, Mutsuko Hatano, Fedor Jelezko, Moriaki Kusakabe, Takashi Yatsui & Masaki Sekino. *Magnetometer with nitrogen-vacancy center in a bulk diamond for detecting magnetic nanoparticles in biomedical applications*. Scientific reports, vol. 10, page 2483, 2020.

[Maertz 10] B. J. Maertz, A. P. Wijnheijmer, G. D. Fuchs, M. E. Nowakowski & D. D. Awschalom. *Vector magnetic field microscopy using nitrogen vacancy centers in diamond*. Appl. Phys. Lett., vol. 96, page 092504, 2010.

[Martínez 20] Felipe Perona Martínez, Anggrek Citra Nusantara, Mayeul Chipaux, Sandeep Kumar Padamati & Romana Schirhagl*. *Nanodiamond Relaxometry-Based Detection of Free-Radical Species When Produced in Chemical Reactions in Biologically Relevant Conditions*. ACS Sens., vol. 5,12, pages 3862–3869, 2020.

[Neumann 15] Thomas Wolf Philipp Neumann, Kazuo Nakmura, Hitoshi Sumiya, Takeshi Ohshima, Junichi Isoya & Jorg Wrachtrup. *Subpicotesla Diamond Magnetometry*. Phys. Rev. X, vol. 5, page 041001, 2015.

[Probst 15] S. Probst, F. B. Song, P. A. Bushev, A. V. Ustinov & M. Weides. *Efficient and robust analysis of complex scattering data under noise in microwave resonators*. Review of scientific instruments, vol. 86, page 024706, 2015.

[Putz 17] Stefan Putz. Circuit cavity qed with macroscopic solid-state spin ensembles. Springer Theses, Vienna, 2017.

[Qnami 20] Technical Note Qnami. *Fundamentals of magnetic field measurement with NV centers in diamond*. https://qnami.ch/wp-content/uploads/2020/12/2020-12-07-Qnami-TN1-The-NV-center-1.pdf, 2020.

[Rondin 14]   L Rondin, J-P Tetienne, T Hingant, J-F Roch, P Maletinsky & V Jacques. *Magnetometry with nitrogen-vacancy defects in diamond*. Reports on Progress in Physics, vol. 77, page 056503, 2014.

[Shammah]   Nathan Shammah. Superradiant light emission (dicke superradiance). Jupyter Notebook. https://nbviewer.jupyter.org/github/qutip/qutip-notebooks/blob/master/examples/piqs-superradiant-light-emission.ipynb.

[Shammah 17]   N Shammah, F Nori, N Lambert & S De Liberato. *Superradiance with local phase-breaking effects*. Phys. Rev. A, vol. 96, page 023863, 2017.

[Suter 17]   Dieter Suter & Fedor Jelezko. *Single-spin magnetic resonance in the nitrogen-vacancy center of diamond*. PNMR, vol. 98-99, pages 50–62, 2017.

[wik]   Wikipedia: Purcell effect. https://en.wikipedia.org/wiki/Purcell_effect.

[Zaitsev 00]   A.M. Zaitsev. *Vibronic spectra of impurity-related optical centers in diamond*. Phys. Rev., vol. B 61, page 12909, 2000.

[Zhou 18]   Sisi Zhou, Mengzhen Zhang, John Preskill & Liang Jiang. *Achieving the Heisenberg limit in quantum metrology using quantum error correction*. Nature Comm., vol. 9, page 78, 2018.